Skoltech
Skolkovo Institute of Science and Technology

Skolkovo Institute of Science and Technology

CARBON NANOMATERIALS: SYNTHESIS AND CHARGE TRANSPORT MEASUREMENTS

Doctoral Thesis

by

ARTEM K. GREBENKO

DOCTORAL PROGRAM IN PHYSICS

Supervisor
Professor Albert G. Nasibulin
Co-advisor
Dr. Dmitry Krasnikov

Moscow - 2022

I hereby declare that the work presented in this thesis was carried out by myself at Skolkovo Institute of Science and Technology, Moscow, except where due acknowledgment is made and has not been submitted for any other degree.

Candidate (Artem Grebenko)

Supervisor (Prof. Albert Nasibulin)

Co-advisor (Dr. Dmitry Krasnikov)

Abstract

Carbon nanomaterials (CNMs) are important both fundamentally and practically. Their modifications (fullerenes, carbon nanotubes or graphene) and their ensembles boosted the science at a certain period of time due to unusual and promising structural and optoelectronic properties. Despite the history of more than 30 years of experimental investigation (in total), they are still highly demanded and more than that these materials represent a great platform to test and develop novel solutions for the CNMs beyond graphitic ones. Mainly, there are three questions that yet have a prospect for deeper understanding: synthesis of CNMs with tailored characteristics, charge transfer in individual nanostructures and ensembles, and eventually design of novel fabrication approaches taking into account the understanding of electronic, mechanical and optical properties. Herein, all these three topics are covered, being closely connected with each other.

The first part of the thesis focuses on the synthesis problems, mainly on chemical vapor deposition of graphene and SWCNT using heterogeneous catalytic disproportionation of carbon monoxide, i.e. Boudouard reaction over a metallic substrate (either nanoparticle or a liquefied metal surface). This part covers studies of previously published aerosol-assisted synthesis of SWCNTs and later adoption of the Boudouard reaction for the graphene synthesis. As a result, an ambient pressure CVD reactor was designed and facilitated single-crystal monolayer graphene grains with up to 5 mm size.

Further, synthesized materials are extensively studied by the means of contactless broadband spectroscopy techniques to characterize and find out new phenomena in the charge carrier dynamics. Observed different spectral contributions were associated with specific processes affecting the charge transfer, like the presence of delocalized carriers, tunnel junctions and defects. These measurements are supported by studying individual carbon nanostructures (individual nanotube or graphene grain) and microscopical investigation of potential spreading. As a result we have observed peculiar features like quantum hall effect in mm-size graphene grains and super poissonian noise in SWCNT quantum dots.

Finally, in the third part, these materials are used for the development of novel techniques for lithographic patterning. One discussed realization is achieved with the help of an atomic force microscope lithography (AFML), which allows dry patterning of optical properties in SWCNT film. This is the first application of AFML to create an optically active medium in SWCNT film by simply controlling its

density in a local manner with 100 nm resolution. The second approach is covered in the form of the review regarding techniques with an enhanced compatibility in terms of the material of patterning.

As a result, novel synthesis techniques of CNM are proposed, and the obtained materials exhibit superior optoelectronic properties, either as is, or thanks to the reported patterning technique.

Publications

1. **A. K. Grebenko**, D. V. Krasnikov, A. V. Bubis, V. S. Stolyarov, D. V. Vyalikh, A. A. Makarova, A. Fedorov, A. Aitkulova, A. A. Alekseeva, E. Gilshtein, Z. Bedran, A. N. Shmakov, L. Alyabyeva, R. N. Mozhchil, A. M. Ionov, B. P. Gorshunov, K. Laasonen, V. Podzorov, A. G. Nasibulin. **"**High-Quality graphene using Boudouard Reaction". **(2022).** *Adv. Sci. n.d., n/a, 2200217.* DOI (https://onlinelibrary.wiley.com/doi/epdf/10.1002/advs.202200217)
   a. Patent: Method of Graphene synthesis, RU 2019120973 dated 04.07.2019
   b. Patent: A Method of graphene transfer on polymer" Russian patent application 2757239 submitted on 22.05.2020.

2. **A. K. Grebenko**, K. A. Motovilov, A. V. Bubis, A. G. Nasibulin, "Gentle patterning approaches towards compatibility with bio-organic materials and their environmental aspects" (**2022**), Invited Review by *Small* Wiley-VCH, DOI (https://doi.org/10.1002/smll.202200476)

3. **A. K. Grebenko**, *et al.*, "Local ultra-densification of SWCNT films: modeling and experiment". Submitted Manuscript (ACS, 2022). arxiv (http://arxiv.org/abs/2203.06387)

4. S. U. Piatrusha, L. V. Ginzburg, E. S. Tikhonov, D. V. Shovkun, G. Koblmüller, A. V. Bubis, **A. K. Grebenko**, A. G. Nasibulin, V. S. Khrapai, "Noise Insights into Electronic Transport". *JETP Lett.* **108**, 71–83 (2018). DOI (https://link.springer.com/article/10.1134/S0021364018130039)

5. G. Drozdov, I. Ostanin, H. Xu, Y. Wang, T. Dumitrică, **A. Grebenko**, A. P. Tsapenko, Y. Gladush, G. Ermolaev, V. S. Volkov, S. Eibl, U. Rüde, A. G. Nasibulin, "Densification of single-walled carbon nanotube films: Mesoscopic distinct element method simulations and experimental validation". *J. Appl. Phys.* **128**, 184701 (2020). DOI (https://aip.scitation.org/doi/10.1063/5.0025505)

6. E. S. Zhukova, B. P. Gorshunov, A. P. Tsapenko, **A. K. Grebenko**, A. V. Bubis, S. S. Zhukov, E. A. Simchuk, V. I. Tsebro, A. A. Tonkikh, D. V. Rybkovskiy, E. I. Kauppinen, A. G. Nasibulin, E. D. Obraztsova, "Charge transport mechanisms in macro-scale CNT films". *J. Phys. Conf. Ser.* **1092**, 012178 (2018). DOI (https://iopscience.iop.org/article/10.1088/1742-6596/1092/1/012178)

7. B. P. Gorshunov, E. S. Zhukova, Ju. S. Starovatykh, M. A. Belyanchikov, **A. K. Grebenko**, A. V.

Bubis, V. I. Tsebro, A. A. Tonkikh, D. V. Rybkovskiy, A. G. Nasibulin, E. I. Kauppinen, E. D. Obraztsova, "Terahertz spectroscopy of charge transport in films of pristine and doped single-wall carbon nanotubes." *Carbon*. **126**, 544–551 (2018). DOI (https://www.sciencedirect.com/science/article/abs/pii/S0008622317310722)

8. E. S. Zhukova, **A. K. Grebenko**, A. V. Bubis, A. S. Prokhorov, M. A. Belyanchikov, A. P. Tsapenko, E. P. Gilshteyn, D. S. Kopylova, Y. G. Gladush, A. S. Anisimov, V. B. Anzin, A. G. Nasibulin, B. P. Gorshunov, "Terahertz-infrared electrodynamics of single-wall carbon nanotube films". *Nanotechnology*. **28**, 445204 (2017). DOI (https://pubmed.ncbi.nlm.nih.gov/28832014/)

Author Contribution

1. The author performed most of the research, wrote the manuscript and both patents.
2. The author performed most of the research and wrote the manuscript.
3. The author performed most of the research and wrote the manuscript.
4. The author performed SWCNT device fabrication and electrical measurements.
5. Author performed experimental verification of the modeled densification verification.
6. The author performed THz, FIR, and KPFM measurements.
7. The author performed THz, FIR, and KPFM measurements.
8. The author performed THz, FIR, and KPFM measurements.

Acknowledgments

Table of Contents

List of Symbols, Abbreviations

AFM – Atomic Force Microscope

AFML – Atomic Force Microscopy Lithography

AP-CVD – Atmospheric Pressure Chemical Vapor Deposition

ARPES – Angle Resolved PhotoElectron Spectroscopy

CNM – Carbon NanoMaterial

CVD – Chemical Vapor Deposition

EBL - Electron Beam Lithography

FIR - Far InfraRed

FTIR – Fourier Transform InfraRed

KPFM - Kelvin Probe Force Microscopy

LEED - Low Energy Electron Diffraction

LFM - Lateral Force Microscopy

MIR - Middle InfraRed

NEXAFS - Near Edge X-ray Absorption Fine Structure

NIR - Near InfraRed

OL - Optical Lithography

QHE - Quantum Hall Effect

STM – Scanning Tunneling Microscope

SWCNT – Single-Walled Carbon Nanotubes

TDS – Time Domain Spectroscopy

THz - Terahertz

XPS - X-ray Photoelectron Spectroscopy

XRD - X-ray Diffraction

Introduction

Low-dimensional carbon nanomaterials (CNMs) became an essential part of the modern semiconductor micro-electronic industry[1]. They are already included in the development roadmaps of the biggest microelectronic companies, such as TSMC, Intel, AMD, and IBM. Experimental observation and subsequent investigation of their properties, including fullerene, single-walled carbon nanotubes (SWCNTs) and graphene can be compared to the discovery of asbestos and plastic - previous historically significant technological miracles that have changed the life of humanity. The knowledge that vitally influences their utilization and application can be divided into three main fields.

The first one is the deep understanding of how to manufacture carbon nanomaterials, i.e. their synthesis. Brilliant conceptual devices that demonstrate state-of-the-art characteristics are of course fundamentally important[2,3], but the real-world applications still require large improvement of the production throughput and chemical purity of the synthesized material. It should be noted that in every case of a laboratory produced material there is a high standard to reach - natural exfoliating crystals. According to the latest reviews the most industrially important approach is chemical vapor deposition (CVD)[4] - a technique that allows formation of various films and crystalline structures using gaseous sources of materials. Focusing on the CNMs reviewed in this thesis, the first industrial large-scale SWCNT production technique HiPCO[5] employed carbon monoxide as a carbon source. Later, aerosol-assisted CVD[6–8] again employing carbon monoxide, has resulted in an outstanding quality of the synthesized material. In its turn SWCNTs, a close sibling graphene within the last decades employed different hydrocarbons[9–13] as a carbon source for CVD successively reaching the quality of exfoliated samples[2]. However, carbon monoxide has not been employed for a monolayer graphene synthesis before, having at the same time the most promising advantages[14,15] that could have largely simplified the set-up and improved graphene quality simultaneously. ***So far carbon monoxide and its disproportionation reaction, i.e. Boudouard reaction, are the heart of CVD approaches utilized in this research to improve existing and develop new synthesis techniques of CNMs***. It is peculiar that the Boudouard reaction has been used for an extensively long time for the synthesis of different carbon materials[16–19], especially a graphitic carbon.

The second implies application of CNMs keeping in mind their unique physical and chemical properties, and so far assumes careful investigation of their electronic properties - both at ambient conditions and subjected to low temperatures and magnetics fields. In case of SWCNTs, e.g., the progress has already reached the solution of global electronic problems claimed in the International Technology Roadmap. These modifications of carbon appeared to solve the problem[20] of the single transistor footprint shrinking below 40 nm several years ago; and all this thanks to the rigorous investigation of the charge transfer peculiarities in these tiny carbon tubes. The same is true regarding graphene - its potential applications are revealed thanks to investigating different peculiarities of charge transfer and quantum behavior of this material. Charge transfer investigation, that helps to understand possible application areas and at the same time to analyze the quality of produced material can be performed in many different ways, and herein we focus on two of them. The first one is the broadband spectroscopy[21], notably terahertz (THz) and far-infrared (FIR) regions of the spectrum, that contain detailed information on the charge carrier dynamics and can be captured without additional fabrication routines to create contacts to the material of study. Typically these spectra can be collected from large (>3 mm lateral size) samples and represent an average observable of nanostructures ensembles in the macrozise system. Interaction of SWCNT networks and graphene films with THz radiation is of critical importance for their implementation in optoelectronic devices. In contrast, the second measurement scenario assumes probing charge transfer properties of an individual element, e.g. a single individual nanotube with metallic contacts. Investigation of electronic properties of nano-objects at low temperatures (<1 K) and in the presence of magnetic fields (up to 7 T) delivers important information on its quality and structure (e.g. quantum hall effect in graphene serves as a classical hallmark feature). ***Therefore, the investigation of charge transfer in both individual CNMs and their ensembles is essentially important to understand generalities in the electron dynamics and features specific for a particular modification.***

Finally, the third field builds up around the fabrication routines. CNMs significantly differ from the conventional 3D semiconductors dominating in the contemporary microelectronics industry and so far novel fabrication techniques are highly demanded. In addition, though SWCNTs and graphene are generally quite compatible with conventional lithography procedures such as electron-beam[22] or optical[23] lithography, nanomaterials beyond CNMs, i.e. metal-organic frameworks, organic semiconductors and

biological nanostructures require much more sophisticated techniques. At the same time, SWCNTs and graphene, being highly-investigated materials, are the perfect platform to test novel solutions. So far, there are two global issues associated with patterning techniques. The first comes from the meshy structure of CNM ensembles, which is mechanically unstable when a liquid is applied[24]. Usual e-beam or optical lithography, therefore, fails to preserve the pristine state of non-patterned areas of the films or layers. Whereas, the dry lithographic concept is prominently represented by atomic-force microscopy lithography (AFML)[25] which is still not completely adopted for the use with nanostructures including CNMs. The second problem is deeper - many organic nanomaterials are highly incompatible with contemporary resists. One of the steps to bring regular routines and obtain enhanced compatibility was earlier done at Skoltech using chitosan derivatives as a resist for electron beam lithography[26]. ***This request formulates the last field of research described here - the development of novel lithographic procedures for CNM ensembles and carbon nanomaterials beyond graphitic carbon.***

To sum up, this thesis is devoted to the synthesis, modification, and investigation of optoelectronic properties of low-dimensional carbon materials: single-walled carbon nanotubes and graphene. The evolution of the electronic properties of materials containing benzene rings as its basis is illustrated employing charge transport measurements, broadband spectroscopy, and scanning probe microscopy. These three approaches are highly supportive of each other and help understand the observed effects more precisely. Some general features are detected in each case, such as a Drude-like delocalized contribution to conductivity, plasmonic resonant absorption, and quantum behavior at low temperatures. Individual unique phenomena that arise in each particular object are studied, e.g., Coulomb blockade in short pieces of SWCNTs and quantum hall effect (QHE) in graphene. Aside from the physical properties of the charge carrier transfer process, synthesis peculiarities both from the chemical and physical sides of view are investigated.

The dissertation begins with the motivation section, briefly introducing the materials. **Chapter 2** gives an extensive overview of the experimental techniques employed in this research. Often experimental results were supported by various computational techniques, so far not mentioned in this thesis but highly acknowledged. **Chapter 3** describes the synthesis procedure of all studied materials, focusing mainly on chemical vapor deposition (CVD) approaches. **Chapter 4** covers charge transfer

peculiarities detected by various measurement techniques including broadband spectroscopy, microscopy and photoelectron spectroscopy methods. **Chapter 5** covers the patterning methods that help modify optical properties of SWCNT films by means of atomic force microscope. Finally, the last chapter briefly summarizes this work via the conclusions, and all published and submitted manuscripts are attached to the end of the present document.

Chapter 1. Scientific Background

1.1 The Carbon Ring

Low dimensional materials reviewed in this thesis have a 6-atom carbon ring as their basis (see **Figure 1**). It goes without saying that even the determination of its structure was a big leap for materials science and chemistry. These rings form 2D lattice in the case of graphene, while the 2D lattice itself can be seamlessly "rolled" into the SWCNT. Its chemical building block is not the only common thing - its structure and carbon nature result in peculiar electronic properties that make such materials fundamentally and practically exciting. There are multiple routes towards synthesizing such structures, including widespread chemical vapor deposition (CVD) techniques, exfoliation, arc-discharge, and many others. Herein, synthesis, investigation, and modification of such samples are presented.
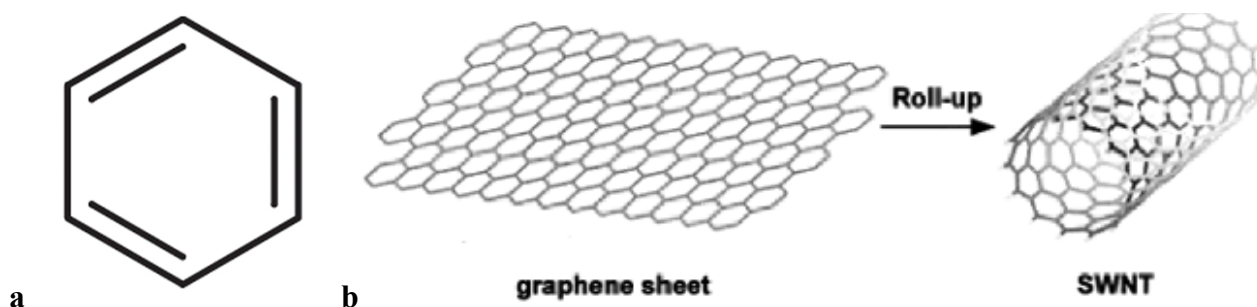
Figure 1. Schemes of the investigated carbon low-dimensional allotropes. (a) - Benzene ring, a basis element in graphene and SWCNTs (shown in (**b**)). (Source - freeimages.com & unsplash.com)

1.1.1 Graphene

Even though historically, single-walled carbon nanotubes were obtained much earlier[27] than the graphene[3], ideologically, this allotrope modification is the best to start with. A single-atom-thick carbon nanosheet first experimentally investigated by Konstantin Novoselov and Andrey Geim[3,28] occurs to be a platform for low-dimensional materials physics and chemistry. This material has a hexagonal honeycomb lattice (schematically shown in **Figure 2**) with a lattice period of 2.45 Å . It is a completely sp^2 hybridized carbon allotrope modification.
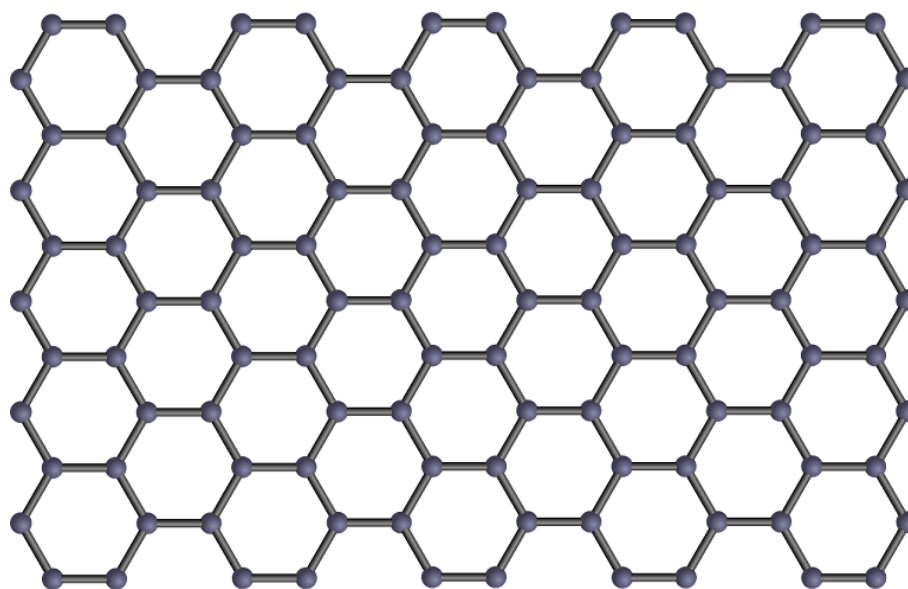
Figure 2. Schematic image of graphene, sp^2 carbon lattice. (Source - freeimages.com & unsplash.com)

Graphene discovery created significant challenges both for device fabrication[28–30] employing properties of these materials and for graphene synthesis[10–12] because its potential industrial application requests for large samples that are out of scope of traditional exfoliation techniques often utilized for prototypes. Moreover, even though there are multiple outstanding approaches towards synthesizing single-crystal monolayer graphene[9,12,31,32], the request for higher quality is still present. Aside from the reaching monocrystalline samples, the key motivation is to deliver the high chemical purity, often lacking in hydrocarbon derived graphene[10,33–35]. In this particular research, we delivered a novel method for graphene synthesis and a comprehensive analysis of its chemical and electronic properties[36]. More results can be found in **Chapter 3** and **4** and in **Paper 1** attached to this thesis.

1.1.2 Single-Walled Carbon Nanotubes

SWCNTs are a few nanometer wide tubular allotropes of carbon, i.e. graphene sheets seamlessly "rolled" into the nanotube. This material was synthesized many times throughout the history of humanity, including the example of damask steel, but was firstly carefully investigated by Iijima et al. back in 90s[27] and since then was permanently studied. Numerous applications were reported, e.g., as cutting-edge

devices made of individual nanotubes[37,38] and as SWCNT networks[39,40] for optoelectronic needs. Being a nano-scale material, carbon nanotubes established a challenge towards its synthesis. The shift from 2D to 1D results in the creation of the large manifold of materials with different properties thanks to van Hove singularities in the density of states spectrum and charge transfer properties dependent on the graphene layer rolling direction. Progress of the last decades resulted in high-quality production of individual nanotubes and their networks with the help of aerosol assisted chemical vapor deposition approaches[7,14,15]. Such a method employs the heterogeneous catalytic decomposition of a carbon source gas on metallic nanoparticles. Herein we present the development of a floating-catalyst (aerosol) atmospheric pressure CVD reactor using various catalyst nanoparticles. We employ SWCNT films created with the help of such reactors to investigate charge transfer peculiarities by means of THz spectroscopy and Kelvin Probe Force Microscopy. We also investigated devices based on an individual nanotube.

The synthesis procedure, samples fabrication and the investigation of optoelectronic properties are covered in **Chapter 3** and **4** and the corresponding **Papers 1,4-8**.

1.2 Atomic Force Microscopy Lithography

AFML is a fastly developing branch of dry lithographic techniques that finds new and unique fields of application. It has already become a key method to create state-of-the-art devices in 2D materials[41] employing capabilities of local electrochemical anodic oxidation. It is also actively used in biochemical problems[25,42], where the application of classical optical and electron-beam lithography can not be considered. Despite the tremendous and widespread efforts and universality of the technique, there are still unsolved or at least unstandardized problems. As an example, application of the AFML with meshy ensembles of CNMs can be mentioned. Herein, we intended to adopt indentation, i.e., direct local physical pressing of the target material with an AFM tip, to control optical properties of SWCNT films. In contrast to previous realizations of AFML, we combined nano-indentation with scanning methods such as HybriD™ and PeakForce tapping™. Doing so, we managed to eliminate the destructive lateral movements of the tip on the mechanically unstable meshy network material. This part of the thesis is deeper covered in **Paper 3** and **Chapter 5**.

1.3 Gentle Patterning Techniques

Earlier we have demonstrated a resist based on chitosan derivatives[26]. The primary goal was to create a resist that would be suitable for use with organic and biological materials. This challenge requests mild processing conditions both regarding physical treatments and chemical reagents applied. While investigating this particular solution, we have inevitably faced the situation, that the final technology always is a trade-off between various parameters, and therefore we performed a deep and exhaustive review on all solutions created on the edge of the last three decades. This review is aimed to help the reader to choose the particular solution among the existing ones depending on the samples' requirements. Also, several pathways to design novel patterning techniques are claimed.

Lithographic techniques are the heart of contemporary microelectonics[1] which actively employ novel materials. The development of graphene[3,28,29] and other 2D materials[43], including contemporary successes in the development of metal-organic frameworks[44–46], organic semiconductors[47–50] and even biological nanostructures[51–54] postulate the need for development of techniques, that assure higher degree of compatibility in terms of physical and chemical treatments following the processing routines. In our paper[55] we deliver an in-depth analysis of the proceedings regarding the development of eco-friendliness, the compatibility degree, and the safety of various lithographic approaches. We describe the advances in optical lithography[56], electron-beam lithography[22], nanoimprint lithography[57],atomic force lithography[58] and try to give the guidelines for the reader to select a suitable approach for the samples of their need. Our own result, the resist based on chitosan-derivatives[26], took an important place in this comparison showing a great performance among the other techniques. For more details, please refer to **Paper 2**, attached to this thesis.

Chapter 2. Experimental Section

2.1 Chemical Vapor Deposition
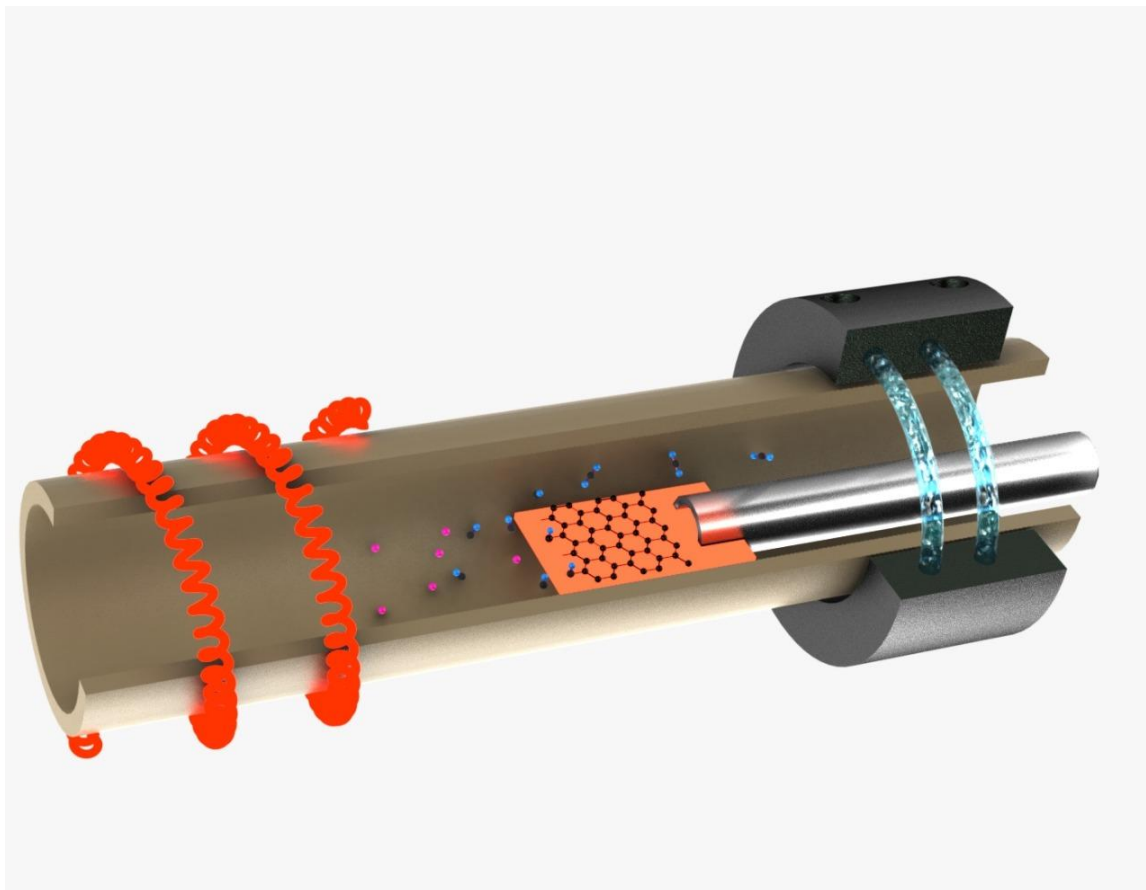
Figure 3. Schematic illustration of a typical CVD reactor. Ceramic or quartz tube is located inside a tubular furnace and with the help of either gaseous inject (for SWCNT floating catalyst synthesis) or with ceramic manipulator (in case of Graphene synthesis) the catalyst is delivered inside the chamber. After subjection to the synthesis environment the sample is removed for further analysis, transfer and investigation.

Chemical vapor deposition (CVD)[4] - is an approach towards the synthesis of various systems, either at the nano- or microscale, that includes deposition of the semiconductor thin films, crystalline structures and polymers. By now, a great manifold of different set-ups has been suggested. They cover the range of ultra high-vacuum[59] stations to the high-pressure large through-put systems[5]. Some solutions even include plasma to enhance the activity of the chemical reagents and generate more radicals. In this research three different CVD reactors are utilized: vertical floating-catalyst CVD reactor for synthesis of SWCNT networks, implemented in our Laboratory[6,8]; horizontal atmospheric pressure CVD (AP-CVD) graphene

reactor built by the author of the thesis, and Parylene-N deposition reactor built by the author and Dr. Anton Bubis. A typical design of a horizontal reactor is illustrated in **Figure 3**. All constructed devices utilized tubular furnace in order to create a heated zone, quartz or ceramic tube i.e. the reactor chamber, set of mass flow controllers to introduce gaseous mixture into the chamber and pressure control unit, represented by either mechanical valve or by a scroll pump to reach desired pressure values. For the case of SWCNTs and graphene we utilized the heterogeneous catalytic disproportionation of carbon monoxide molecules as a source of carbon during synthesis. We typically used either metallic nanoparticles, or metallic substrates as a catalyst. Elevated temperatures ensured optimal conditions for the reaction. Parylene-N deposition was non-catalytic - in this case we used two-zone horizontal tube furnace to ensure sublimation (zone 1) and decomposition (zone 2) of the paracyclophane (in a certain way - p-xylene dimer molecule), which individual units later polymerized in the cold zone of the reactor exhaust. CVD techniques are actively used in contemporary industry and are simultaneously developed and adopted to new materials and composites.

2.2 Nano-Fabrication

2.2.1. Graphene Samples
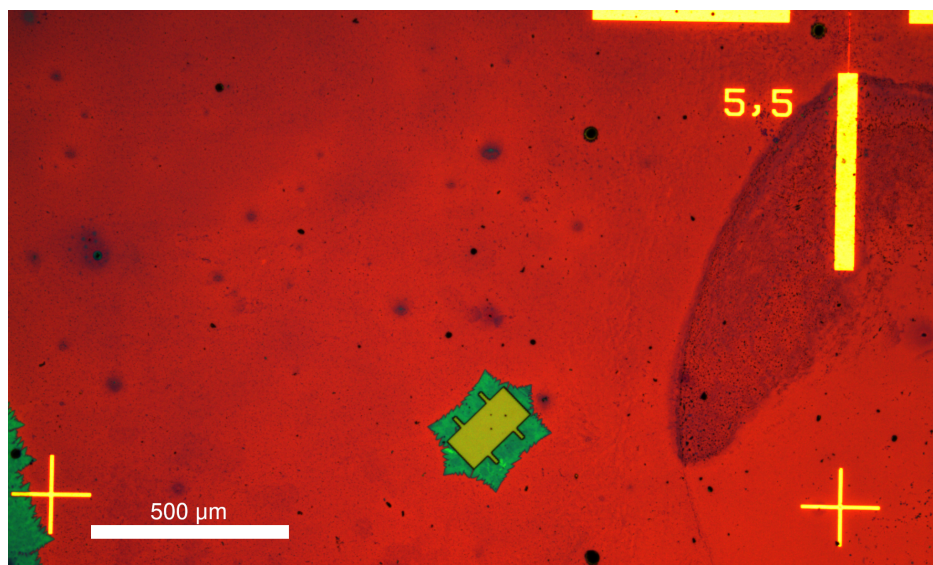
Figure 4. Typical design of the graphene hall-bar structure after lithographic patterning and before O_2 plasma etching. Green color - encapsulated graphene, yellow - hall bar mesa formed from resist, red - parylene-N, bright yellow - deposited Au landmarks.

In order to investigate quantum effects in a graphene system we designed a novel method for graphene transfer. Due to the fact that the catalyst forms a single crystal during the resolidification procedure, it was impossible to utilize bubble-transfer technique[60]. Great adhesion between atomically smooth single crystal copper surface and graphene allowed delamination only at the voltage range when the graphene layer was highly damaged. So far, we had to utilize chemical etching of the catalyst layer, and as far as it also contained molybdenum foil we utilized a universal etchant: 30 ml H_3PO_4, 18 ml HNO_3, 10 ml CH_3COOH, 65 ml H_2O, which was able to dissolve both large piece of copper and molybdenum foil within approximately 12 hours. Utilization of this etchant was impossible together with classic supporting layers such as PMMA or cellulose acetate, so far we adopted the route towards utilization of parafilm[61] and parafilm/parylene-N hybrid.

Graphene transferred by such a method (typically individual crystals of >1 mm lateral size) were encapsulated into Parylene - N layer. To do so, firstly the target substrate of Si/SiO_2 was covered by roughly 30 nm parylene, and the transfer procedure was held in an inert gas glove-box (N_2, <0.1 ppm of water, <0.1 ppm of oxygen). After that, graphene placed on Parylene-N was annealed in high vacuum conditions at 300 ℃ to remove the contaminants. The vacuum chamber is connected to the glove box, therefore after the annealing procedure was completed, the sample was loaded out again into an inert atmosphere. Finally, the sample was placed in the reactor chamber, sealed, transferred out of the glove box, connected to the parylene-N reactor and the sample was encapsulated by an additional 40 nm layer.

After that, regular optical lithography using Heidelberg uPG direct laser write system was employed to pattern hall-bar structures out of individual grains. We used AZ 1245 resist together with LOR 5B underlayer to ensure high quality of lift-off. Parylene-N was easily etched with the help of oxygen plasma. We designed the hall-bar geometry (see **Figure 4**) so that the border is highly developed and therefore a larger length contacts the metallic contacts.

2.2.2 Individual SWCNT Devices

In order to fabricate devices using individual SWCNTs we firstly prepared Si/SiO_2 wafers with Au/Ti landmarks by means of electron beam lithography. We used the CABL Crestec 3000 e-beam lithography station at the Center for Collective Use of Moscow Institute of Physics and Technologies. These wafers with landmarks were later subjected to the outlet of floating catalyst CVD reactors tuned to

the low throughput regime - so far we obtained wafers with randomly oriented sparse nanotubes. They were further localized with the help of AFM relative to the landmarks. AFM was chosen to minimize destructive impact coming from electron beam in SEM. Finally, these nanotubes were patterned with the help of AR-P CSAR 6200 resist. Contacts were deposited in high vacuum conditions (vacuum better than $3x10^{-7}$ mbar) after overnight pumping. Typically 0.4 nm of Ti and 59 nm of Pd were used.

2.2.3 SWCNT Films

SWCNT films were synthesized using a floating catalyst (aerosol) chemical vapor deposition method in a vertical hot-wall tubular reactor[6,8,15] heated to 850 ℃. Ferrocene was used as a catalyst precursor, which vapor was delivered from a saturator (cartridge containing ferrocene and granular silica mixture) to the reactor hot zone by a gas flow. Carbon monoxide was utilized as a carbon source and a gas carrier simultaneously, while a small amount of CO_2 (~1 vol%) was added into the reactor for nanotube growth promotion.[62] SWCNTs were grown in the aerosol phase and collected downstream of the reactor using a nitrocellulose filter and afterward transferred to the target substrate through the dry transfer technique[7]: a filter with SWCNT film was applied to the surface of the substrate, dry-pressed, and released.

2.3. Microscopy

2.3.1. Atomic Force Microscopy

Atomic force microscopy was one of the key instruments for sample analysis after synthesis, during fabrication steps, and, as well, one of the vital techniques to measure electronic properties of the nanomaterials. Mainly two devices have been employed during this study - Bruker Multimode V8 and NT-MDT Next II. Atomic Force Microscope operating in Quantum NanoMechanical Mapping (™) implemented in Bruker Multimode V8 was found to be extremely useful for the visualization of graphene grains on the surface of the copper foil, shown in **Figure 5**.
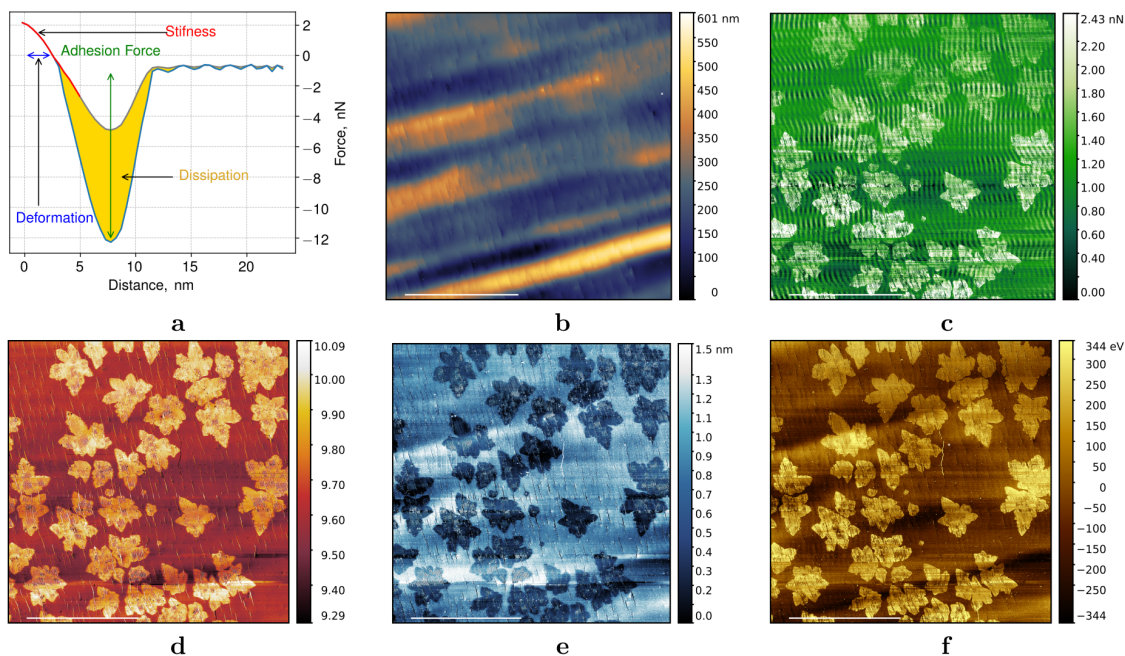
Figure 5. QNM visualization of graphene grains. a, Typical force-distance curve captured by AFM operating in a PeakForce tapping regime. All useful parameters are indicated. Topography (**b**), adhesion force (**c**), Young modulus (**d**), sample's deformation (**e**) and cantilever's dissipation energy (**f**) for the same very region of the Cu-foil with graphene grains. While grains are completely invisible in the topography channel, they are clearly seen in all other mechanical channels due to the impact of material contrast. Scale bar is 50 micrometers.

In contrast to a typically widespread modes of AFM operation, PeakForce tapping collects much more information within a single scan - when the tip is correctly calibrated and its parameters are suitable for this particular sample in terms of DMT theory[63], one can capture maps of Young Modulus, Adhesion interaction properties and sample deformation. Results of this method application for the case of copper foil with graphene grains are shown in **Figure 5**. While the grains can be hardly seen in the topography channel (**Figure 5b**), the contrast is much better in any other feature like Young Modulus and Adhesion Force maps (**Figures 5c** and **d**).

This approach has not been utilized for graphene grain visualization before. It may be useful in case of other substrates as well. Even though this approach is less favorable in case of conductive copper foil substrate, when compared to conventional Scanning Electron Microscopy (SEM) imaging, its potential

can not be underestimated in case of dielectric or polymeric substrate, when an SEM can not be utilized. It delivers comparable imaging quality and contrast with a broader list of compatible materials. Often graphene is combined with materials that have a developed surface with roughness and overall height difference much larger than the single layer thickness. This fact makes it impossible to have a clear imaging utilizing simply topographical contrast.

For the lithographic patterning we have mostly employed Next II microscope, as it supports vector and raster-based lithography patterning in any possible way: applying force, voltage or current.

2.3.2. Kelvin Probe Force Microscopy

Kelvin Probe Force Microscopy[64] (KPFM) has been realized in a non-standard two-pass regime. The first path, when the topography of the sample is captured, was done with the help of PeakForce tapping, which resulted in a higher precision of the height determination, when compared to standard amplitude tapping. The second path, when the tip was lifted and the potential was measured, employed common tip oscillations at the resonant frequency of the cantilever (driven by applying AC electromagnetic field). Deeper insight is schematically shown in **Figure 6**.
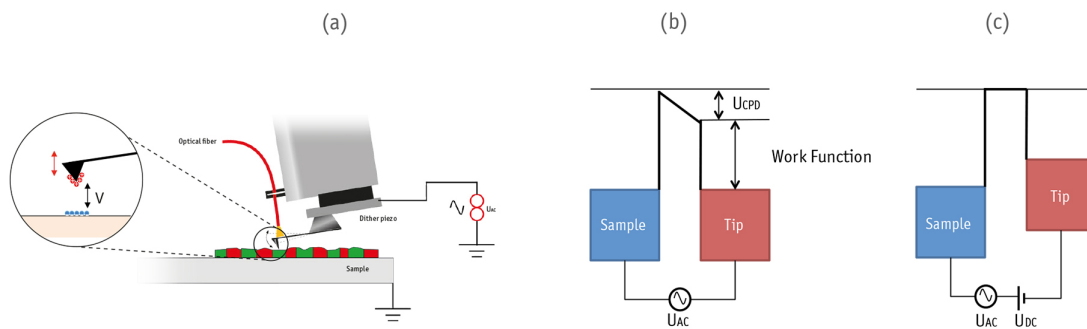
Figure 6. **Basics of KPFM**. **(a)** First, an AFM tip scans the sample's topography. On the next step, the tip is lifted up for a fixed distance and follows the same line recalling all topographic features. At each point of scan, tip oscillations are driven by an electrical field - applied AC voltage (**b**), and DC voltage is used to minimize the amplitude of these oscillations (**c**). DC voltage that facilitates this minimization is directly connected with the work function of the investigated material, and if appropriate conditions are utilized and the tip's work function is calibrated by a known material even quantitative data can be captured.

In this research standard, lifted-mode KPFM was utilized in order to investigate SWCNT films. Firstly, in each line of scan, topography was captured. After the line was captured, the tip moved back to the beginning, lifted up for a fixed distance (50-70 nm typically) and went through the same line repeating the previously captured topography. At this moment tip oscillations are driven with the help of an AC electrical field. Simultaneously in each point of scan DC voltage is applied to the tip. The DC voltage value at which the oscillations' magnitude turns zero is directly connected with the sample's work functions.

2.3.3. Optical Microscopy

A Leica optical microscope was utilized to visually control the sample's quality. Typically, images were collected using 10x, 20x and 50x objectives. Images were processed with the help of fiji (FIJI is just imageJ, recursive name) to contrast images and perform statistical analysis.

2.3.4. Electron and Ion Microscopy

The structure and distribution of samples were investigated by scanning electron microscopy (SEM) (FEI Versa 3D) under the conditions of secondary electrons detection mode (ETD detector) and 10 kV electron beam accelerating voltage. We also used Jeol JSM-7001F at acceleration voltages from 10 to 30 kV. Secondary electron images of SWCNT films were recorded using the Zeiss Orion Plus helium ion microscope at an acceleration voltage of 30 kV. The ion-induced electron emission allows imaging morphological details, similarly to a secondary electron microscope. Compared to electron microscopy, the reduced penetration and scattering of helium ions allow a better spatial resolution down to ~ 0.5 nm. The chamber pressure was $3x10^{-7}$ Torr during imaging, and the typical ion beam current was 1.3 pA. A transmission electron microscope (TEM) FEI Tecnai G2 F20 was used to investigate the structure of SWCNTs. To minimize the destructive influence of electron irradiation all measurements were performed at the acceleration voltage of 80 kV and with minimal possible electron illumination time. SWCNTs were directly collected at the reactor outlet onto carbon coated gold TEM grids.

2.4 Broadband Spectroscopy

2.4.1 UV-vis Spectroscopy

UV-vis spectrometer Perkin Elmer Lambda 1050 was utilized for visible and UV range transmittance spectra capture. Typically, the sample and its substrate were captured separately against air and processed with the help of python packages. UV reflection was measured with a custom micro-spectrometer using frequency-doubled Ti:Sapphire laser as a light source. UV light was loosely focused onto the sample using an underfilled 20x plan-fluor objective lens. The illumination spot diameter at the sample was approximately 15 μm. Spectra of the reflected radiation were captured with the Solar S100 spectrometer providing 1 nm spectral resolution. Scattering spectra were measured in a transmitted-light microscopy setup with Köhler illumination. Light from a halogen lamp was focused to the back-focal plane of a plan achromat objective with NA of 0.25. Transmitted and scattered light beams were collected with a water-immersion plan apochromat objective with numerical aperture of 1.2. A pair of lenses after the objective were used to create an image of the back-focal plane of the collecting objective. A central stop placed at the position of the back-focal plane image blocked the directly transmitted light and allowed only the scattered radiation to pass. The latter was then coupled to a multimode fiber with an achromatic lens and directed to an Ocean Optics USB4000 spectrometer.

2.4.2 NIR - MIR - FIR Spectroscopy

The Bruker Vertex 80V was used for obtaining NIR-MIR-FIR transmissivity spectra. Room temperature measurements of terahertz spectra and far infrared spectra were performed on a Teraview TPS Spectra 3000 time-domain terahertz spectrometer and Bruker Vertex V80 FTIR spectrometer, respectively. To aware impurity sorption from the atmosphere the measurements were carried out inside CryoMech commercial cold-finger cryostat with Mylar windows after 1 day vacuumization at lower than $5 \cdot 10^{-6}$ mbar pressure. Spectroscopic data were collected with Opus and TPS Spectra software and processed using least-square fitting procedure with the home-made WASF software. Deep minima at higher frequencies correspond to absorption lines of parafilm©. The spectrum of the parafilm was processed using a well-known expression for transmissivity of the plane-parallel layer[21] with the absorption minima modeled with Lorentzians. The obtained electrodynamic parameters of parafilm were employed for least-square fitting of the transmission coefficient of graphene on parafilm using

corresponding expression for two-layered systems. The decrease towards low frequencies of the oscillating transmission coefficient signifies metal-like character of CNM conductivity: lower transparency of the spectrum at low frequencies corresponds to larger conductivity of the film - typical feature in the frequency dependence of AC response of metals/conductors.

2.5 Low Temperature Transport Measurements

2.5.1 Graphene Gate Traces and Quantum Hall Effect

Under ambient conditions, transfer curves have been captured with the help of a probe station and Keysight B1500A Semiconductor Analyser. Low temperature measurements were carried out in a ^{4}He cryostat (4.2 K) where a sample was in the vapor of ^{3}He (exchange gas). Before cooling down an insert with the sample was pumped during > 5 hours with residual pressure $< 5 \cdot 10^{-4}$ mbar. Either standard four-probe low-frequency lock-in or DC techniques were used for electrical transport measurements.

2.5.2 Coulomb Blockade and Shot Noise Measurements

Throughout the experiment, the dc bias voltage with a small ac modulation was applied to the source contact via the input of a home-made I−V converter (10^7 V/A). The current was measured using standard lock-in technique at 31 Hz modulation frequency. The resonant tank-circuit with the central frequency of 20.9 MHz and a 5 kΩ load resistor was connected to the source for the shot noise measurements. As usual, the signal was calibrated using Johnson–Nyquist noise thermometry. We used side gates to check that Coulomb coupling between the two quantum dots on either side of the central contact is negligible, hence possible charging events on the right QD are irrelevant for the transport and noise measured in the left QD. All the data discussed below are obtained at a bath temperature of 0.5 K in a liquid ^{3}He insert with all other gates grounded.

2.6 Photoelectron Spectroscopy

2.6.1 X-ray Photoelectron Spectroscopy

XPS spectra were collected by XPS spectrometer Kratos Axis Ultra DLD with spherical sector analyser, ion gun, ultraviolet and x-ray sources. Experiments were conducted under ultra-high vacuum $5 \cdot 10^{-10}$–$3 \cdot 10^{-9}$ Torr utilizing the irradiation of AlK_α(mono) 1,486.69 eV (energy resolution 0.48 eV, binding energy calibration on Ag $3d_{5/2}$ line).

2.6.2 X-ray Absorption Near Edge Structure

Room temperature NEXAFS measurements were performed at the Russian-German dipole beamline of the BESSY-II electron storage ring operated by Helmholtz-Zentrum Berlin für Materialien und Energie. NEXAFS spectra were recorded in Total Electron Yield (TEY) mode. The measurements were performed for the as-loaded as well as for the annealed (~300 ℃) samples of graphene on copper.

2.6.3 Angle Resolved Photoelectron Spectroscopy

ARPES measurements were carried out using linearly polarized undulator radiation at the U112-2-PGM beamline of BESSY-II in Berlin. Photoelectrons were detected with a Scienta R8000 analyzer at the "One square" ARPES instrument, and the base pressure of the experimental setup was better than 1×10^{-10} mbar. The angular and energy resolutions of the photoemission experiments were 0.1°and 10 meV, respectively. The sample was introduced to the UHV chamber from the atmosphere, and before measurements, it was annealed at 300 ℃ for 20 minutes. During the measurements, the sample was kept at 20 K.

2.7 Raman Spectroscopy

Raman spectroscopy was performed with the DXRxi Raman Imaging Microscope equipped with x50 objective and a 532 nm excitation laser operating at 1 mW output power. Raman spectra were measured at several points along with the sample with the exposure time.

Raman spectroscopy was also performed with a confocal scanning Raman microscope Horiba LabRAM HR Evolution (HORIBA Scientific, France). All the measurements were carried out using: linearly polarized excitation at a wavelength of 532 nm, a diffraction grating with 1800 grooves per millimeter, and an objective with the magnification of 100x and N.A. = 0.90 (Olympus Microscope Objective M Plan N, Japan). The laser spot size was ~ 0.5 μm. To register a significant signal-to-noise ratio, the unpolarized detection was used. Not to initiate any damage to the samples, the Raman spectra were recorded with the laser power set to 100 mW but passing through the neutral density filter set to 5%: no sample damage was observed during the measurements. For statistics, the spectra of each sample were collected at least in 3 different points of the sample: the standard deviation between the spectra was negligible. The acquisition time of 1 sec at each point was utilized with the accumulation of at least 5 times per point.

2.8 Structural Methods

2.8.1 X-ray Diffraction

Diffraction experiments in reflection geometry have been performed at Institute of Solid State Physics of Russian Academy of Sciences (RAS) using monocrystal diffractometer Oxford Diffraction Gemini equipped by CCD detector with resolution of 0.35 A. MoK_α radiation with wavelength of 0.7136 A was used. Further X-ray Diffraction experiments were executed at beamlines No.2 and No.4[65] of VEPP-3 storage ring at Siberian Synchrotron and Terahertz Radiation Center, Budker Institute of Nuclear Physics of Siberian Branch of RAS, Novosibirsk, Russian Federation. The beamline No.2 is dedicated for powder diffraction experiments with high instrumental resolution and is equipped with Si(111) channel-cut monochromator, sample holder moving along Θ angle and Ge(111) crystal-analyzer mounted in front of scintillation detector on the 2Θ arm of the diffractometer. The working wavelength is 0.154 nm. The beamline No.4 operates with a wavelength of 0.03685 nm and the diffracted radiation is registered by 2D image plate detector MAR345. The sample is set in transmission mode and can be rotated around the axis perpendicular to the incident beam.

The experiment at beamline No.2 was carried out in different modes including conventional Θ-2Θ scanning, 2Θ scanning at fixed Θ angle of 4°, Θ scanning at fixed 2Θ positions corresponding to Cu(111) and Cu(200) reflections, scanning with sample spinned around normal to the surface. The diffraction patterns of the sample were obtained at beamline No.4 both in conventional transmission mode with no sample movement and with the sample rotated around the horizontal axis within the range of 30°.

2.8.2 Low Energy Electron Diffraction

LEED embodied in Kratos Ultra DLD was used for tracking the crystallinity of the samples. The distortion of the image, clearly seen from the imperfection of the hexagons formed in the diffraction pattern of the graphene, is caused by the form of the lens, non-flat samples' surface and edge effects of the signal capturing camera.

2.8.3 Electron BackScattering Diffraction

Dual beam scanning electron microscope Helios G4 (Advanced Imaging Core Facility, Skoltech) was used to capture EBSD maps. These maps were further analyzed with the help of python software and color mapped accordingly.

Chapter 3. Chemical Vapor Deposition

3.1 SWCNT Synthesis

Floating catalyst CVD approach utilized in this research was presented by two types of the reactor with a main difference in the principle of catalyst nanoparticles formation. The first one utilizes spark-discharge generation of the nanoparticles from the electrode material[66], as depicted in **Figure 7**. The second uses a ferrocene cartridge[6] as a source of catalytic particles. Carbon monoxide disproportionation on top of these metallic nanoparticles facilitates synthesis of single-walled carbon nanotubes in the hot zone of the reactor.
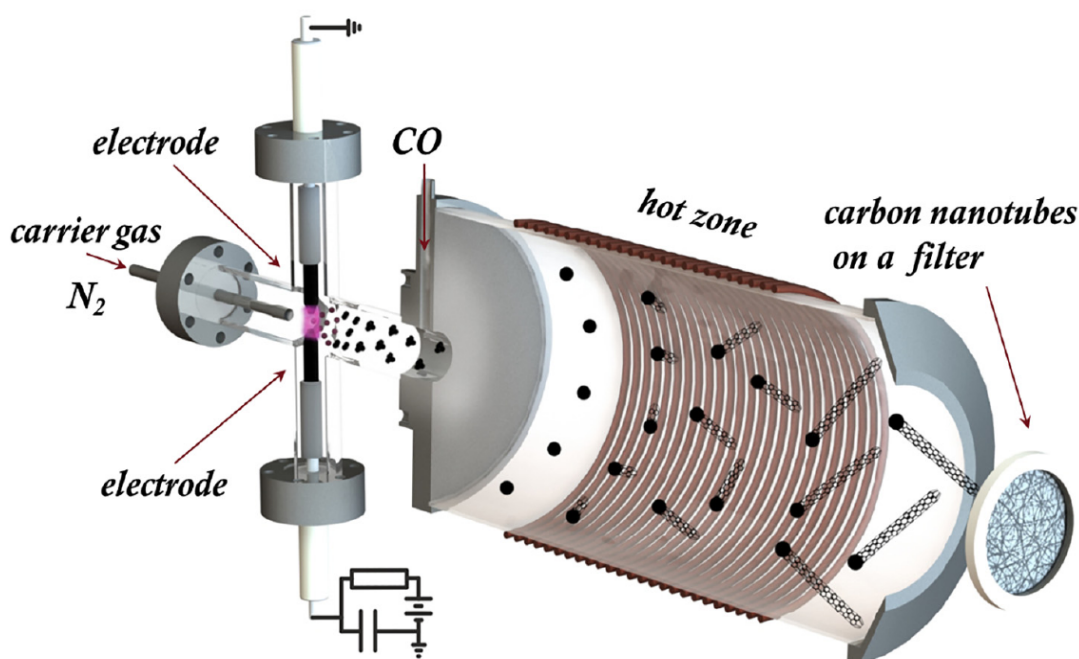
Figure 7. Schematic illustration of an floating catalyst spark-discharge reactor - one of the utilized in this research alongside with an aerosol reactor equipped with ferrocene cartridge.

Synthesized carbon nanotube networks were firstly collected on the surface of the nitrocellulose filter and afterwards transferred on to a target substrate by dry press technique[7].

By such an approach, we have fabricated samples with individual nanotubes deposited in a sparse form and SWCNT films with the thickness up to 1.5 µm on top of arbitrary substrates. Of course, these samples also contained a significant amount of the catalyst nanoparticles which, however, did not

influence the final sample properties. The author of this thesis participated in the reactor optimization[6,66] analyzing the output product by means of AFM, but did not construct the device. Later, the experience with carbon monoxide utilization for SWCNT synthesis was applied to produce graphene, described in the next subsection.

3.2 Graphene Synthesis

In contrast to SWCNTs, for the case of graphene synthesis, the author of this thesis has built the experimental set-up shown in **Figure 8**.
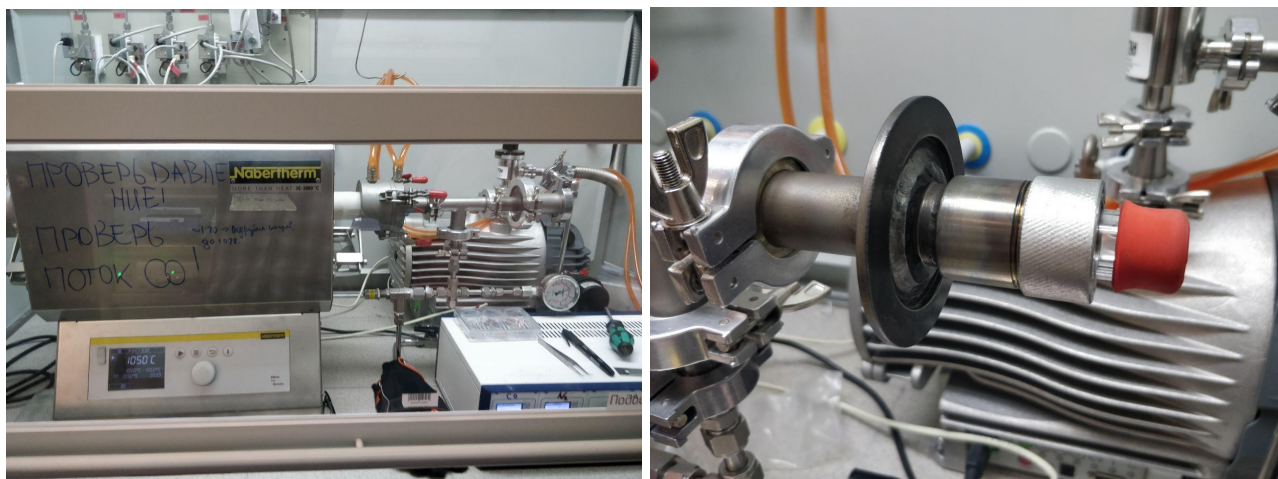
Figure 8. Photos of the graphene AP CVD reactor with fast load-in/out system (right panel) implemented for this project.

In order to speed up the synthesis process, a special load-in/out manipulator has been implemented combining Quick-Connect flange together with regular KF-50 flange. Such a system allowed the use of a tubular quartz manipulator to move the catalyst copper sample from and to the hot-zone of the furnace. At the same time, this part was designed so that after insertion of the holder, the reactor chamber can be sealed up to the inner pressure of 3 atmospheres. Pressure can be precisely controlled with the help of mechanical overpressure relief valves. Altogether, such a design allowed to shorten synthesis time from several hours (including heating and cooling time of the furnace) to tens of minutes.

As it has already been stated in the introduction we have intentionally chosen the path of carbon monoxide utilization as a carbon source for graphene synthesis. Utilization of Boudouard reaction for graphene synthesis allows several beneficial outcomes:

1. In contrast to the hydrocarbon route, carbon monoxide does not require lower pressure to reduce synthesis of amorphous carbon. Even though there are several reported techniques with fine tuned parameters that can operate at ambient pressure for the case of methane, the process should be stopped before a complete monolayer is formed - otherwise there is a high probability of the second layer formation.

2. Methane requires hydrogen for graphene synthesis both for reducing the copper catalyst and for growth rate amplification. In the case of carbon monoxide there is no need for hydrogen, as carbon monoxide itself is a great reducing agent and the pyrolysis process is blocked by unique thermodynamics of CO molecules.

3. Carbon dioxide can be "naturally" used as an carbon etching agent in Boudouard reaction. More than that, addition of a small amount of CO_2 allows synthesis rate control as shown further. Finally, it has been reported as a much more efficient gas for cleaning procedure for the catalyst preparation[67].

4. Carbon monoxide synthesis is flow independent and can be easily utilized in a high-pressure regime with a standing gas. However, this feature requires ultimate purity of the utilized gasses and high sealing of the reactor chamber.

5. Furthermore, aside from the Boudouard reaction, there are several other possible synthesis routes that result in formation of dielectric underneath the graphene layer during the synthesis procedure[68,69].

Deeper analysis of the results is published in "High-Quality Graphene using Boudouard Reaction" by Grebenko et al. (**Paper 1)**. Hereinafter, we will focus only on the synthesis kinetics and structural properties of the synthesized samples. Electronic band structure and charge transfer peculiarities are reported in **Chapter 4**.

3.2.1 Graphene Growth Kinetics
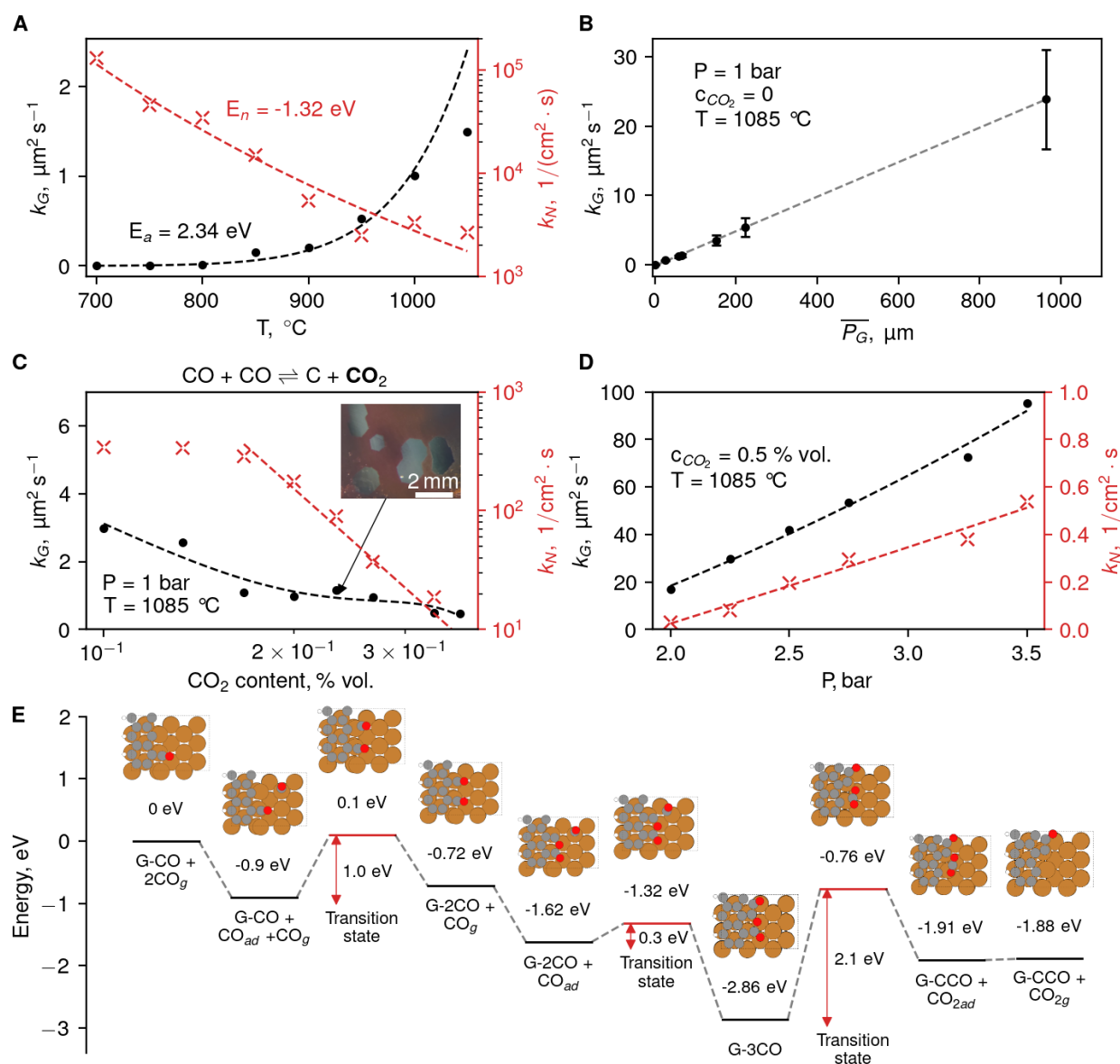
Figure 9. Kinetics summary on graphene synthesis. (A) Temperature dependence of the growth (k_G) and nucleation (k_N) rate. Activation energies and Arrhenius fits ($\ln(k) \propto 1/T$, dashed lines) are indicated on the plot. **(B)** Dependence of the growth rate on the average nucleus perimeter. **(C)** Equilibrium shifting of the Boudouard reaction by addition of carbon dioxide to the synthesis chamber. Note that y-axises have different scales. **(D)** Dependence of the growth and nucleation rate on the reactor's chamber pressure. **(E)** Results of DFT calculations indicating the limiting reaction energy barriers for 100 surfaces. It should be noted that this figure is presented in another format and units in the **paper 1**.

Kinetics investigation of carbon monoxide graphene deposition allowed us to understand physicochemical principles behind the synthesis procedure and to tune it so that single-crystal synthesis can be approached. Our experiments have traditionally begun with Puratronic 99.999% pure copper foils. We started the investigation with the determination of a limiting reaction activation energy for the growth and the nucleation processes. To find out these parameters we firstly heat-treated foil-chunks at 1050 ℃ in Ar/CO_2 gaseous mixture to clean the surface, reduced the furnace temperature to target value and replaced the atmosphere with pure carbon monoxide. We have terminated synthesis when a statistically significant amount of graphene grains were synthesized.

Further we captured several regions with the help of Scanning Electron Microscopy (SEM) or Atomic Force Microscopy (AFM) operating in Quantum Nanomechanical Mapping and processed images with the help of Fiji (Fiji is just imageJ, recursive name). Obtained particle statistics were used to define growth rate k_G and nucleation rate k_N. Dependence of these rates on the synthesis temperature plotted in the form of Arrhenius plots was utilized to obtain activation energies. Those plots are indicated in **Figure 9A**. Activation energy determined from these plots is 2.34 eV for growth process and -1.32 eV for the nucleation. Careful analysis of the samples morphology in SEM and AFM revealed that the developed rough surface of copper foils even subjected to various cleaning and polishing procedures resulted in a high nucleation rate and moreover in the formation of multilayer structures nearby various apexes and protrusions.

In order to overcome this issue we followed an approach of the molten copper substrate utilization[70,71] and replaced foil chunks with pieces of the samely pure copper resolidified on the surface of molybdenum foil used as a wetting layer. Carbon monoxide disproportionation terminates when the catalyst is completely liquefied and so far we worked in the narrow vicinity of the melting temperature - 1085 ℃. This act resulted in a one order of magnitude suppression of the nucleation rate. Further, we have analyzed the dependence of the growth rate on the average nucleus perimeter, illustrated in **Figure 9B**. Talking simply - larger grain growth faster. This finding assumes a possible route of the nucleation suppression in order to make room for individual grains to grow to a large size single-crystal graphene.

Boudouard reaction, $2CO \rightleftharpoons C + CO_2$, allows equilibrium shifting by an addition of carbon dioxide to the synthesis atmosphere. It occured that low concentrations of CO_2 added to a flow of CO significantly

dropped the nucleation rate by 3 orders of magnitude, while the growth rate was mildly reduced by a factor of 2. These results are summarized in **Figure 9C**. Such an approach alone facilitated the possibility of mm-size single crystal graphene synthesis by simply a long synthesis time (~ 1.5 hours) process. Operation at the elevated pressure at the same may speed up the growth reducing the required time to 10 minutes. Growth and nucleation rate dependence on the total pressure in the reactor's chamber is shown in **Figure 9D**. Density Functional Theory calculations performed by professor Kari Laasonen at Aalto University, Finland, helped to understand in detail the limiting reaction rates and energy barriers. Surprisingly, the graphene nucleus edge catalyzed the growth alongside with copper resulting in a barrier of 2.1 eV that coincides well with experimentally observed values: apparent activation energy and linear dependence of the growth rate on the graphene grain perimeter.

3.2.2 Structural Properties
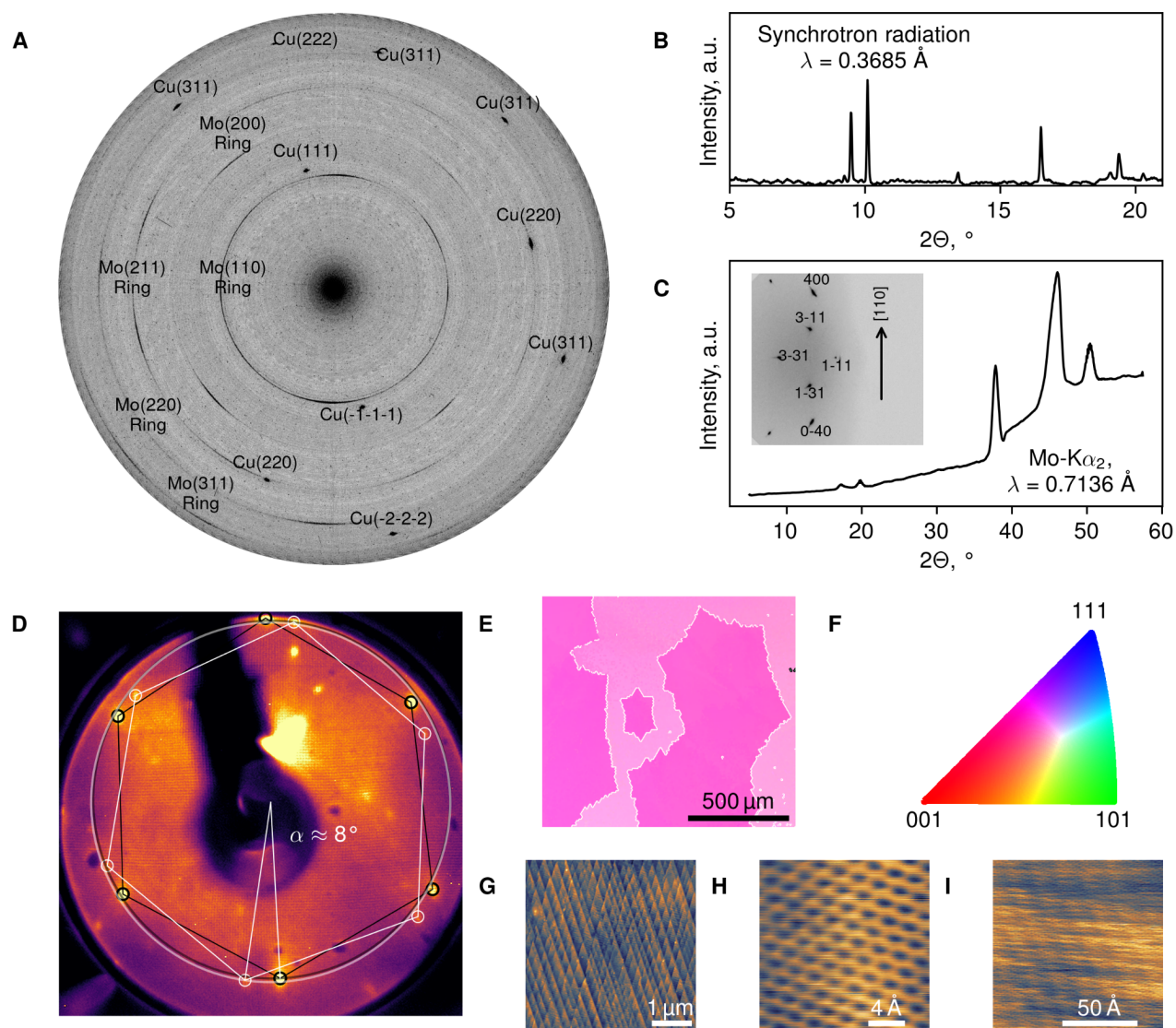
Figure 10. Graphene - copper structure. (A) XRD diffractogram obtained in the transmission geometry. Bright reflexes coming from the copper monocrystal are indicated in the panel. **(B)** The same data presented in the averaged over the azimuthal angle form. **(C)** XRD captured in reflection geometry from another sample synthesized in the same manner. **(D)** Low-energy electron diffraction captured from an individual mm-size graphene grain on the copper substrate. **(E)** Electron Backscatter Diffraction map in the form of IPF. Light areas are not covered with graphene. **(F)** Color-coding legend for IPF. **(G)** AFM image of the copper-graphene topography. The observed steps are approximately 1.5-3 nm high. **(H)** Atomic resolution STM image of the graphene lattice. **(I)** Moire pattern form due to the lattice misalignment.

In order to understand structural features of the synthesized material we performed rigorous investigation employing different techniques. Even though copper pieces utilized in this research were not single crystals and more than that they were resolidified, and as a wetting agent polycrystalline molybdenum foil was used, the whole catalytic substrate occurred to be single-crystalline as determined by a monocrystal diffractometry in transmission and reflection geometries shown in **Figure 10 A-C**. Such unprecedented alignment can not be explained simply by the presence of graphene on top of the copper substrate, as earlier reports on the CVD synthesis of graphene did not observe such phenomena. Most probably, this feature originates from the interaction of carbon monoxide molecules with the surface of the catalyst during crystallization and somehow induces the formation of copper single crystal[72].

Laue diffraction allowed us to determine that the 111 lattice vector is oriented at roughly 10-11° to the surface normal, which is consistent with earlier reported instability of main lattice cuts of copper in the carbon monoxide atmosphere[72]. Further we utilized low energy electron diffraction (LEED, **Figure 10D**) in order to probe the crystallinity of the graphene grains formed in low nucleation regime. Diffraction pattern contained two almost identical hexagons rotated by approximately 8 degrees[73,74] which is one of a typical copper-graphene lattice mismatch angle.

Electron Backscatter Diffraction (EBSD, **Figure 10 E-F**) also has shown an extreme degree of the copper lattice alignment both under graphene grains (darker regions) and outside (light regions). We have also analyzed several other regions on the sample's surface and all of them have shown a similar picture. It should be noted that usually EBSD data does not look so aligned for most of earlier reported CVD graphene. Microscopic analysis revealed that the copper surface is corrugated and forms a stepped surface as can be seen from the AFM image in **Figure 10G**. Deeper analysis of the surface with the help of ultra high vacuum scanning tunneling microscopy (STM) has independently verified the lattice of graphene on top of the sample and visualized the Moire pattern that comes from the twist between copper 111 lattice and graphene.

After we have successfully synthesized high-quality graphene we aimed at the sample's encapsulation and therefore built an additional reactor for Parylene-N deposition.

3.3 Parylene-N Deposition

Parylene, or poly-para-xylene is a widely industrially used polymer, which applications include but not limited to electronic circuits protection from moisture, corrosion and for insulation; bio-acceptable coverage of the devices that are permanently implanted into the body; low-dimensional materials encapsulation for the protection from atmospheric contaminants. It is transparent in a broad optical range and its deposition approach facilitates uniform isotropic covering of the samples under ambient conditions. Deposition process consists of para-xylene dimer sublimation, subsequent decomposition and repolymerization on the surface of a target substrate.
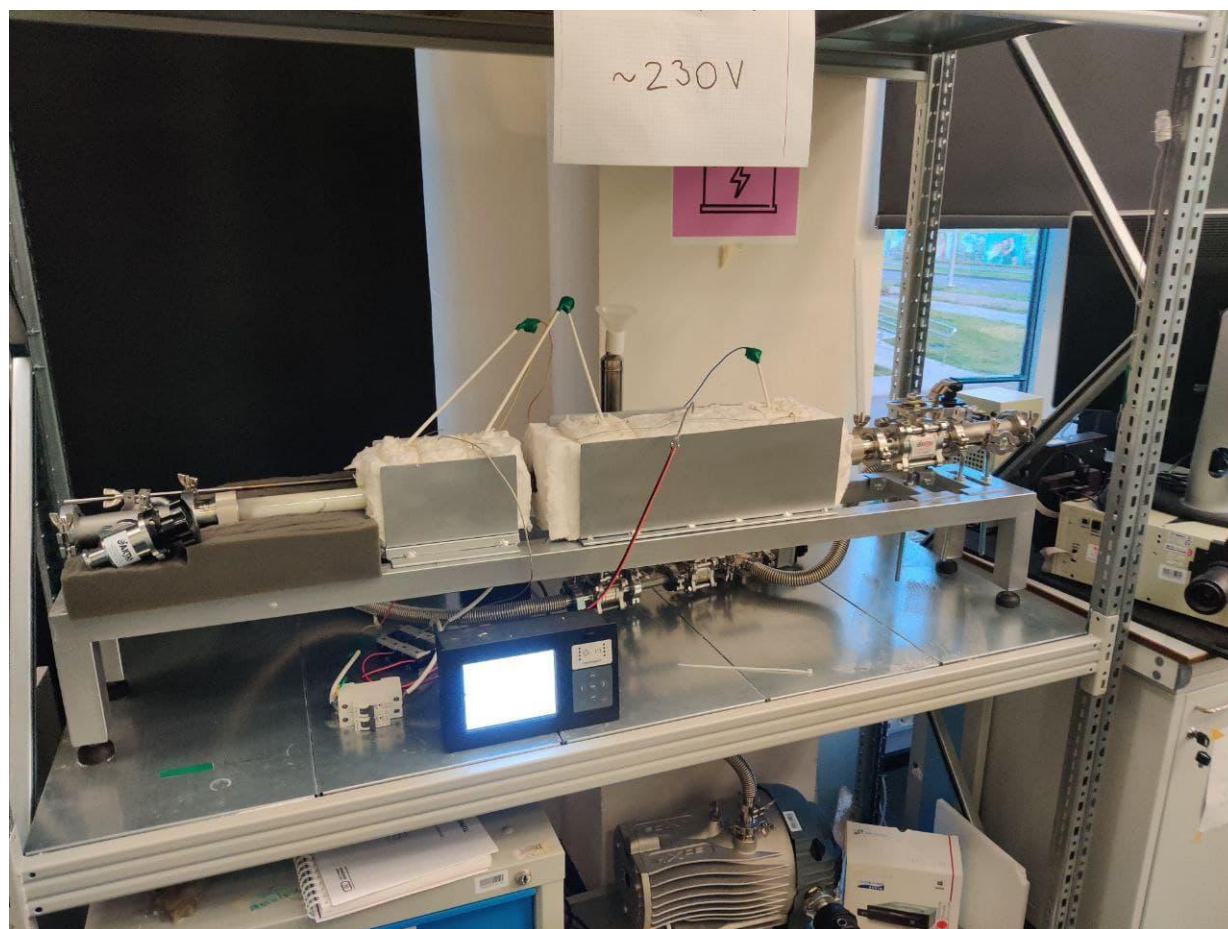

Figure 11. Photograph of two-zone horizontal tubular home-built reactor for deposition of Parylene-N and -C.

To allow it, a two-zone reactor is utilized - two horizontal furnaces with a single quartz-tube reactor chamber (see **Figure 11**). The first zone is kept at 120-175 ℃ and a glass container with parylene dimer is

placed inside the quartz tube exactly at this heated region. Reactor designed so that pumping can be performed from each side of the quartz tube; thus it is possible to precisely control the deposition process and heat-treatment stabilization because of this feature. After the polymer source is loaded, generation of its vapors is stabilized within several minutes, and the pumping removes all vapors so that they do not reach the decomposition zone. Temperature of the first zone allows control of the deposition rate. The second furnace is located right after the first one, and is heated to 620-750 ℃. Here the dimer decomposition occurs. A valve separating the sublimation-decomposition zone of the reactor and room-temperature deposition chamber is used to keep the substrate away from the non-stabilized vapors of parylene precursor and to stop the deposition process upon reaching the desired thickness. Both ends of the quartz tube are connected to a three-exit splitter through individual valves. The third exit of a splitter is connected to a liquid-nitrogen cold trap that protects the pump from parylene contamination. During the stabilization procedure, the valve that goes to the deposition chamber and valve between the deposition chamber and decomposition zone are closed. After the stabilization is complete, pumping from the polymer source side is closed, and both valves from the previous step are open. Normally, 175 ℃ for the first zone and 750 ℃ for the second were set resulting in c.a. 25 nm/s deposition rate and 3-5 nm roughness. However, it is important to note that the deposition rate depends on the substrate's material - for e.g. in the case of graphene, deposition rate drops to 5 nm/s when compared to Si/SiO_2 substrate or copper foil.

Parylene molecules can be chemically modified, in this thesis we have utilized two types: Parylene-N and Parylene-C, the latter has a monomer modified with chlorine atoms, as shown in **Figure 12**.
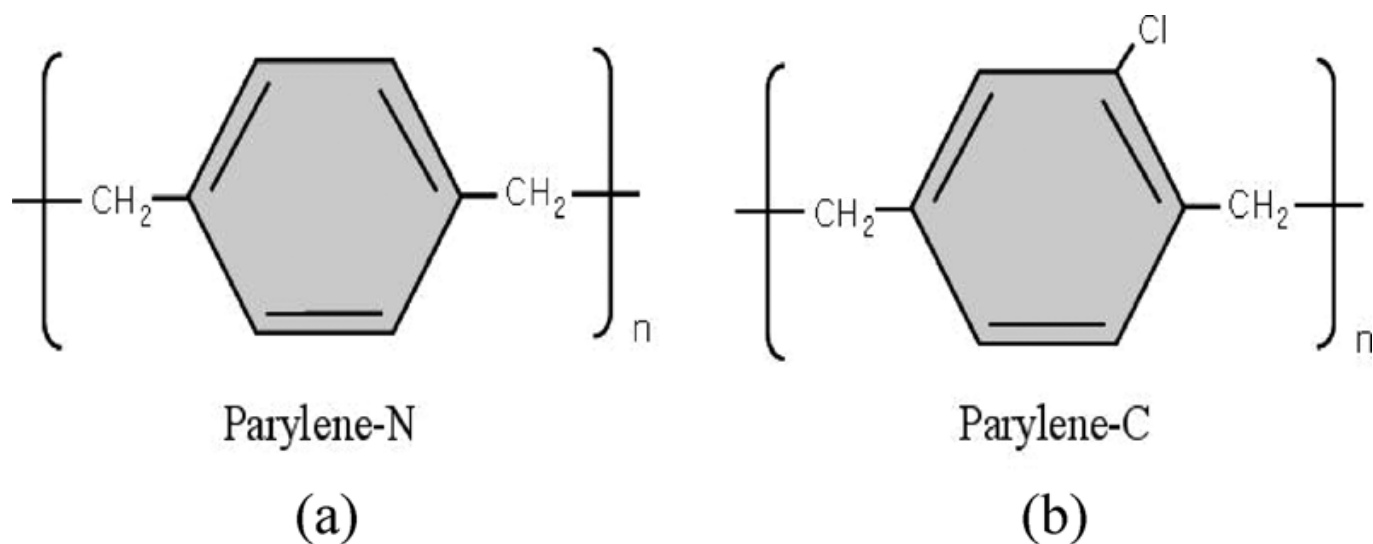
Figure 12. Two types of polymers - Parylene-N **(a)** and Parylene-C **(b)**

This material in terms of the presented research is interesting as it is one of the most compatible dielectric for graphene encapsulation[75]. It produces great protection from H_2O and O_2 and almost does not influence charge carrier concentration levels. Parylene-N withstands heating up to 450 ℃ and therefore allows annealing procedures required for transferred CVD graphene improvement.

This reactor was used for creation of graphene Hall-bar structures to measure the field-effect mobility and quantum hall effect. The reactor chamber allowed it to perform all the transfer manipulations in the N_2 glove box and transfer sealed graphene samples to and from the Parylene reactor.

Samples produced with the help of these three reactors were further investigated in Chapter 4 regarding the charge carrier transfer peculiarities and used for the design of novel patterning techniques in Chapter 5.

Chapter 4. Electronic Properties

For each object of the investigation we either applied different existing scanning probe microscopy techniques, investigated by contact-less and regular charge transfer measurements techniques and searched for hallmark quantum features of the object.

4.1 SWCNTs

4.1.1 Atomic Force Microscopy
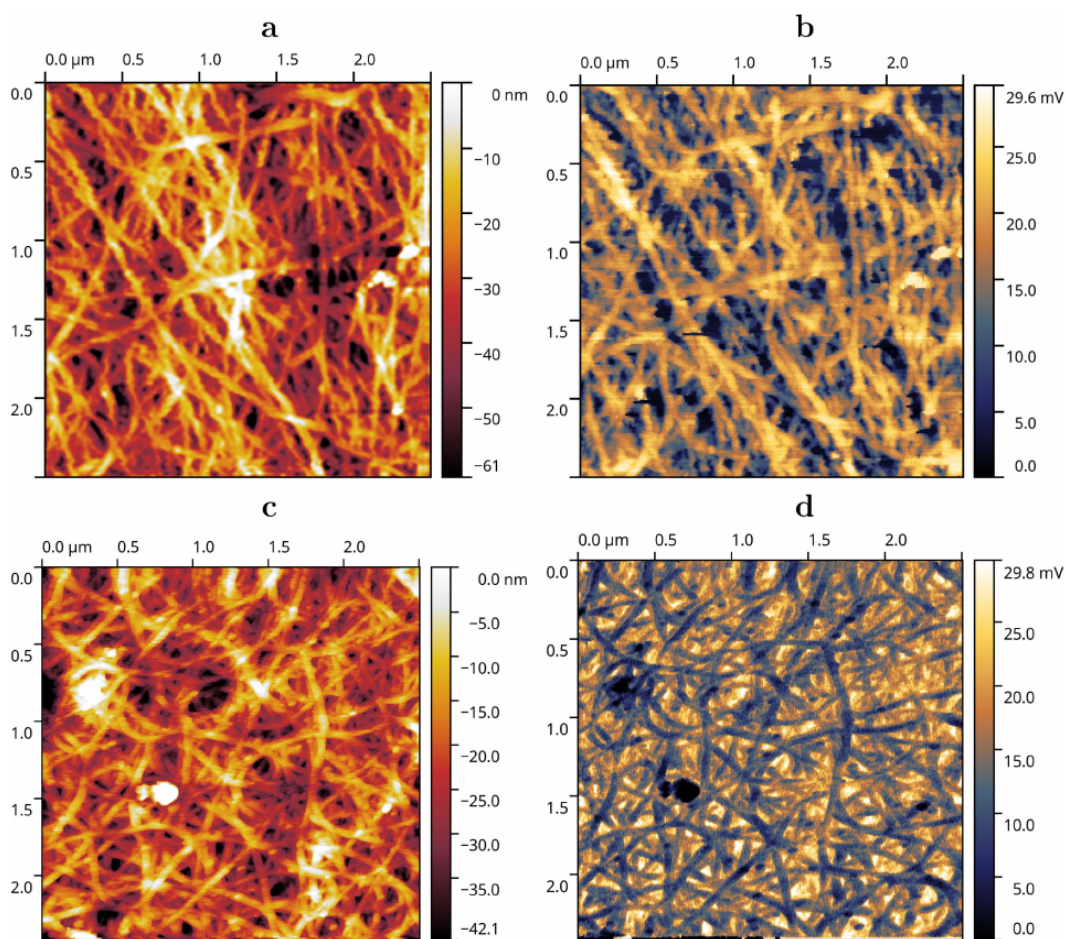
Figure 13. Kelvin-probe force microscopy of SWCNT films. The left column contains the topography channel, and the right one provides information on the work function of the nanotubes. **a,b** correspond to the pristine nanotubes and **c,d,** to the $AuCl_3$ doped film.

When investigating pristine and AuCl₃ doped carbon nanotubes we have utilized KPFM to track the change and distribution of the work function in the sample of 80% transparent SWCNT film as shown in **Figure 13**. These results have shown that in both cases, the distribution of the work function is uniform except the re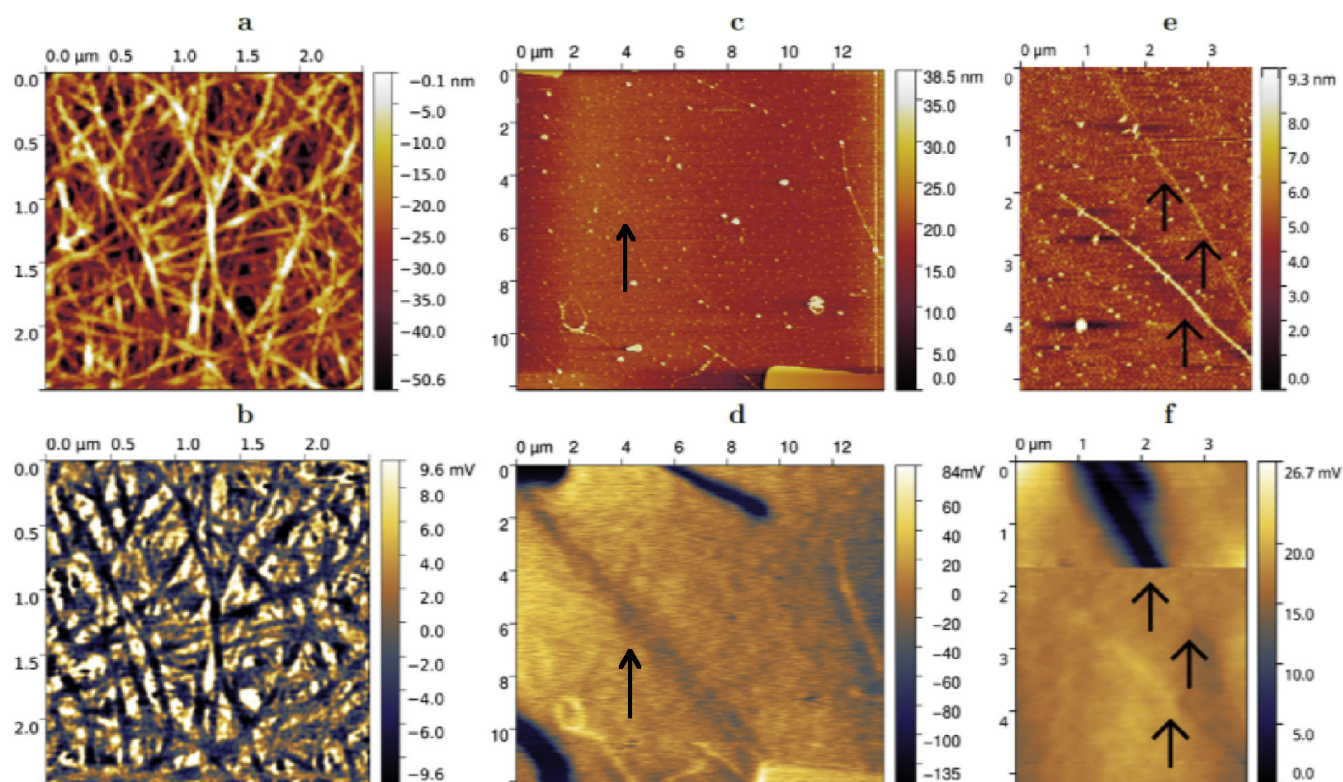gions of individual SWCNT intertube contacts, whose contribution to the determined value is minimal. These data were used to clarify and support the findings made from spectroscopic investigation[76,77].

Figure 14. Kelvin-probe force microscopy of SWCNT films and individual nanotubes. Top row indicates the topography channel, and the bottom shows work-function distribution. **a,b -** KPFM of the pristine SWCNT film. **c,d** Example of individual SWCNT two-terminal device with potential gradually changing from negative (top electrode, panel **d**) to the positive (bottom electrode, panel d). It is an example of deffectless device with adequate electronic behavior at room temperature. The SWCNT is indicated by arrow. **e,f -** Example of defective/contaminated device, where along the channel potential accidentally drops.

Another example of KPFM utilization that demonstrates potential spreading in SWCNT systems is shown in **Figure 14**. In this case aside from SWCNT networks individual two-terminal devices were

studied as well. **Figure 14 c**,**d** illustrate the gradual change of the potential along the nanotube's length when no contamination or defect is present in the channel. In contrast, damaged or contaminated nanotubes demonstrate sharp potential drop as shown in **Figure 14 e,f**. These results were used to support spectroscopic findings concerning the charge transfer peculiarities, i.e. the observed additional absorption lines associated with tunneling processes and inner tube crossings[78]

4.1.2 Broadband Spectroscopy

Time-domain terahertz spectroscopy combined with far-infrared fourier-transform spectroscopy represent a powerful tool for investigation of various electronic peculiarities in the system of interest[21]. In this section we primarily investigated charge transfer peculiarities in conductive SWCNT films, both pristine and chemically modified. Broadband spectroscopy allowed us to clarify that the electromagnetic response of SWCNT films is mostly governed by free charge carriers. Total contribution can be divided into three types:

1. Drude-like contribution of delocalized electrons and holes.

2. Plasmon oscillations of carriers trapped into intersections of individual nanotubes presented in the form of resonance absorption at ~ 100 cm^{-1}.

3. Gap-like absorption at or below 10 cm^{-1} originating from tunnel barriers again at the intersections of the tubes.

The Terahertz region was captured by the means of TeraView TPS time-domain spectrometer (2-100 cm^{-1}) and stitched with spectra collected from far-infrared Fourier spectrometer Bruker Vertex 80v (80-24000 cm^{-1}). FTIR data was later processed using Kramers-Kronig analysis in order to obtain the real and imaginary part of the signal (for the case of TPS both quantities are captured experimentally). For low temperature measurements cryostat with mylar windows was utilized for THz spectra. Main results are illustrated in Figure **15** for pristine and doped SWCNT films. Surprisingly, in case of $AuCl_3$ doping the overall behavior of SWCNT films does not change. These findings are in agreement with KPFM data presented in the previous section.
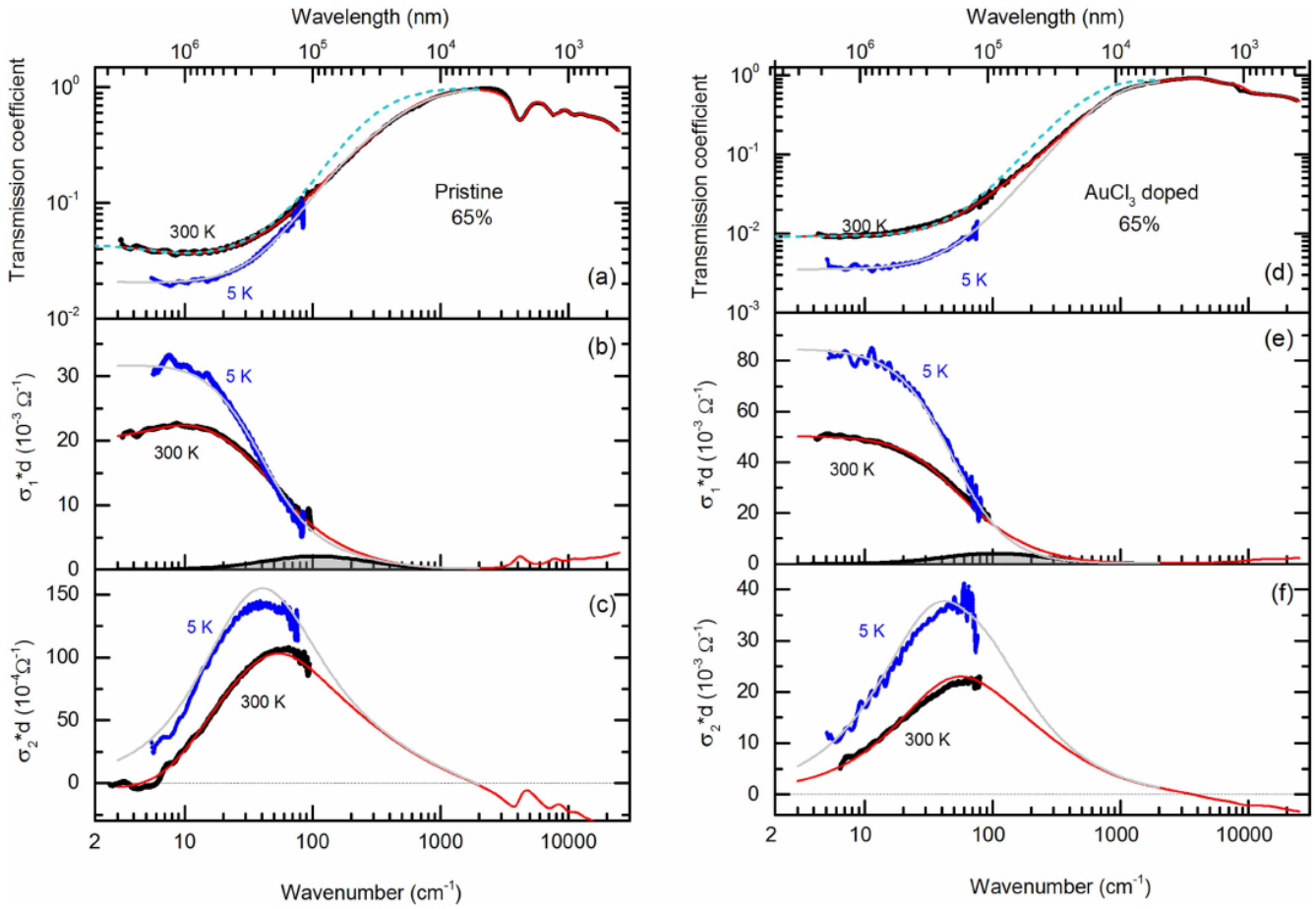
Figure 15. Broadband and THz spectroscopy of SWCNT films. Black circles and lines are used for room-temperature spectra, and blue circles are used for low temperature (5 K) spectra. **a,d -** transmission coefficient, **b,e** - real and **c,f** - imaginary part of conductance for pristine (left column) and AuCl$_3$ doped nanotubes. Gray filled region corresponds to the plasmonic oscillations, while frequency independent region of the real part is attributed to Drude-like conductivity with free carriers.

Deeper insight into the data analysis of spectroscopic results is presented in **Paper 6,7** and **8** presented in this thesis[76–78]. This spectral behavior will be further compared to the THz-FIR spectroscopy of graphene samples. Further, such SWCNT films were also compared to iodine and CuCl doped

SWCNTs in the same manner. Results of a broadband spectroscopy are shown in **Figure 16.**
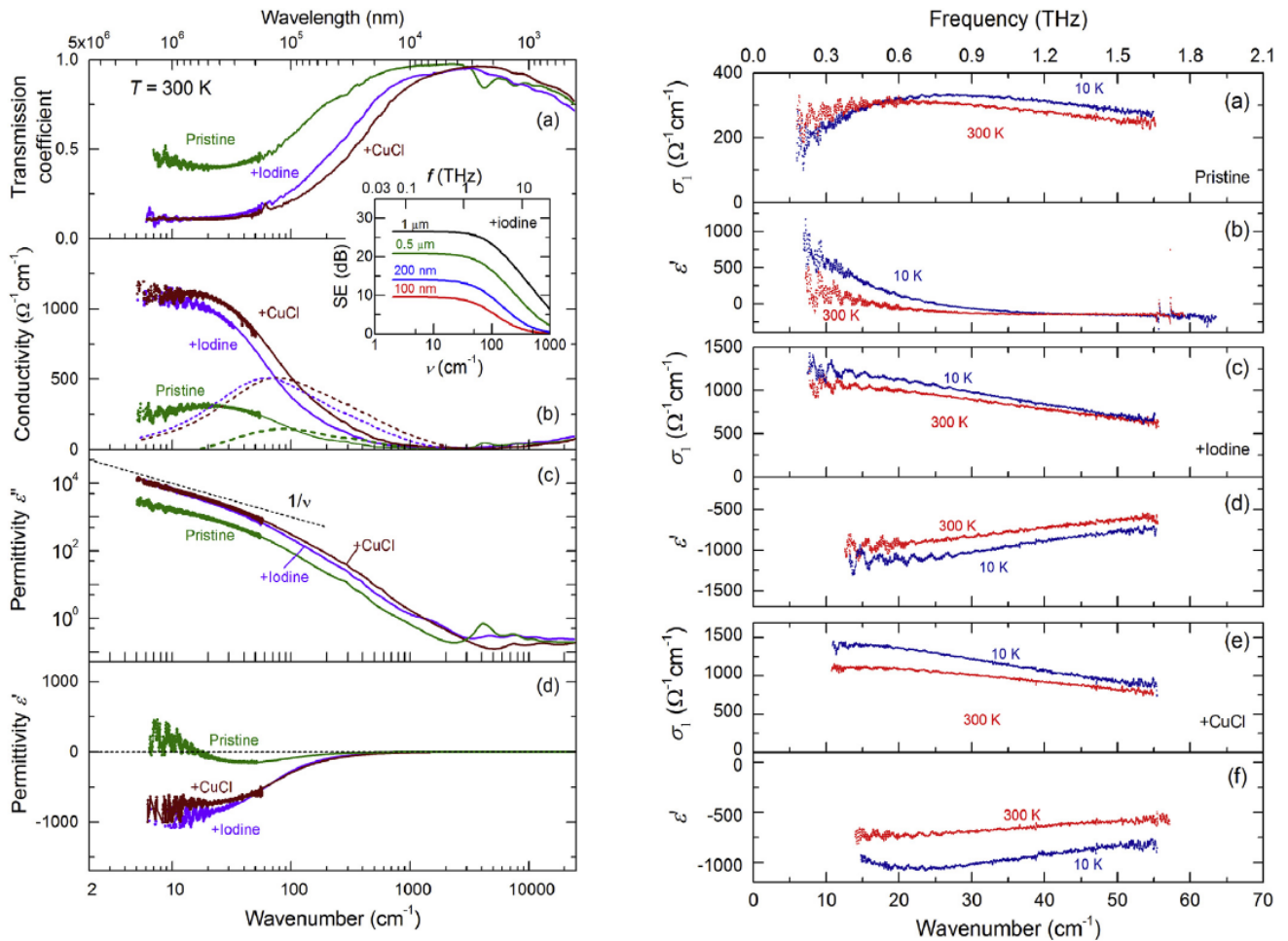
Figure 16. Broadband and THz spectroscopy of SWCNT films. Left: Room temperature spectra of transmission coefficient (a) at terahertz (dots) and infrared (lines) frequencies of three SWCNT films, pristine, CuCl- and iodine-doped. Infrared spectra of real (solid lines in panel b) and imaginary (dashed lines) parts of the conductivity and imaginary (c) and real (d) parts of the permittivity were obtained by spectral analysis of the transmission coefficient spectra, as described in the Paper 8. Dots in panels (b, c, d) correspond to the directly measured THz values of conductivity and permittivity. Straight dashed line in panel (c) indicated metallic dependence of the imaginary part of the dielectric permittivity, expression (2). The inset shows shielding effectiveness SE = -10log(Tr) (Tr – transmission coefficient) for the iodine-doped film calculated for different thickness using the measured spectra of conductivity and permittivity. **Right:** Terahertz spectra of conductivity (a, c, e) and real permittivity (b, d, f) of pristine, CuCl- and iodine-doped SWCNT films, measured at room temperature and at 10 K.

4.1.3 Coulomb Blockade

Individual SWCNTs have very low electrical capacitance which make them a great candidate for creation of a Quantum Dot (QD), when measured at low temperatures. Short region of a carbon nanotube confined between two metallic contacts with Schottky barriers (which naturally form tunnel barriers) represents almost ideal QD - a conductive island weakly coupled to macroscopic electron rich terminals. This structure is fabricated with the help of classical electron-beam lithography and electron beam evaporated Ti/Pd/Au (0.3/5/60 nm) metallic contacts (shown in the inset of **Figure 17**). There were two interconnected QD in the fabricated device, each approximately 400 nm long.
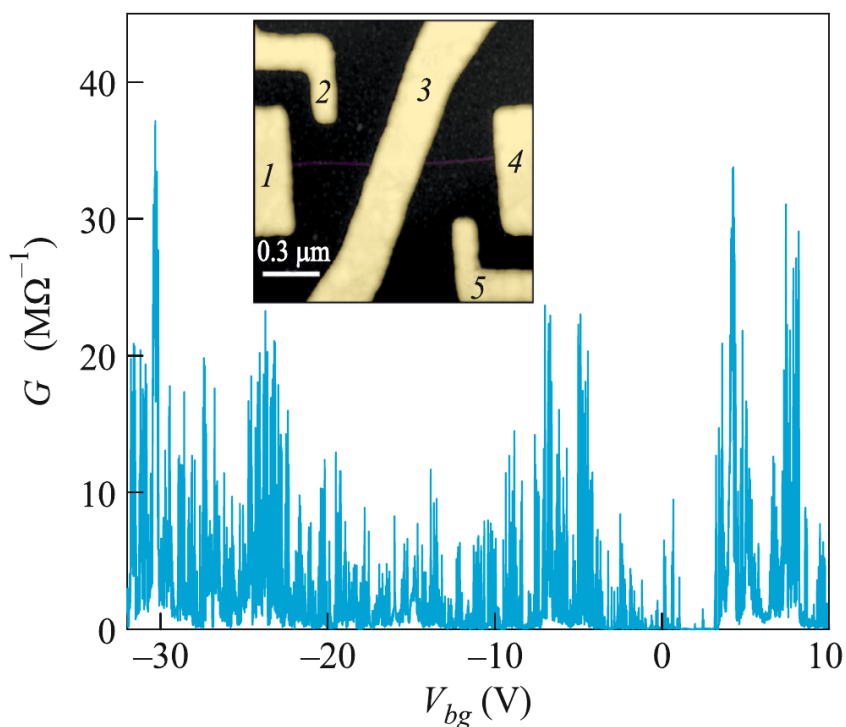
Figure 17. Transconductance curve of an individual SWCNT operating in Coulomb blockade regime. Differential conductance plotted as a function of a back-gate voltage (V_{bg}) captured from the left segment of the device shown in the inset (contacts 1 and 3).

Within almost the whole back-gate voltage range Coulomb blockade oscillations with irregular amplitudes are pronounced. Narrow region of V_{bg} [1, 3] V depicts the energy gap in the spectrum typical of a semiconducting nanotube. For well-defined oscillations when the ratio between maximal and minimal conductance is at least 10, finite bias spectroscopy has been performed (see **Figure 18**)

indicating the additional energy of the order of 1-5 meV. Such behavior is not expected for an individual nanotube, and it may be used as another proof that the investigated structure is a SWCNT bundle.
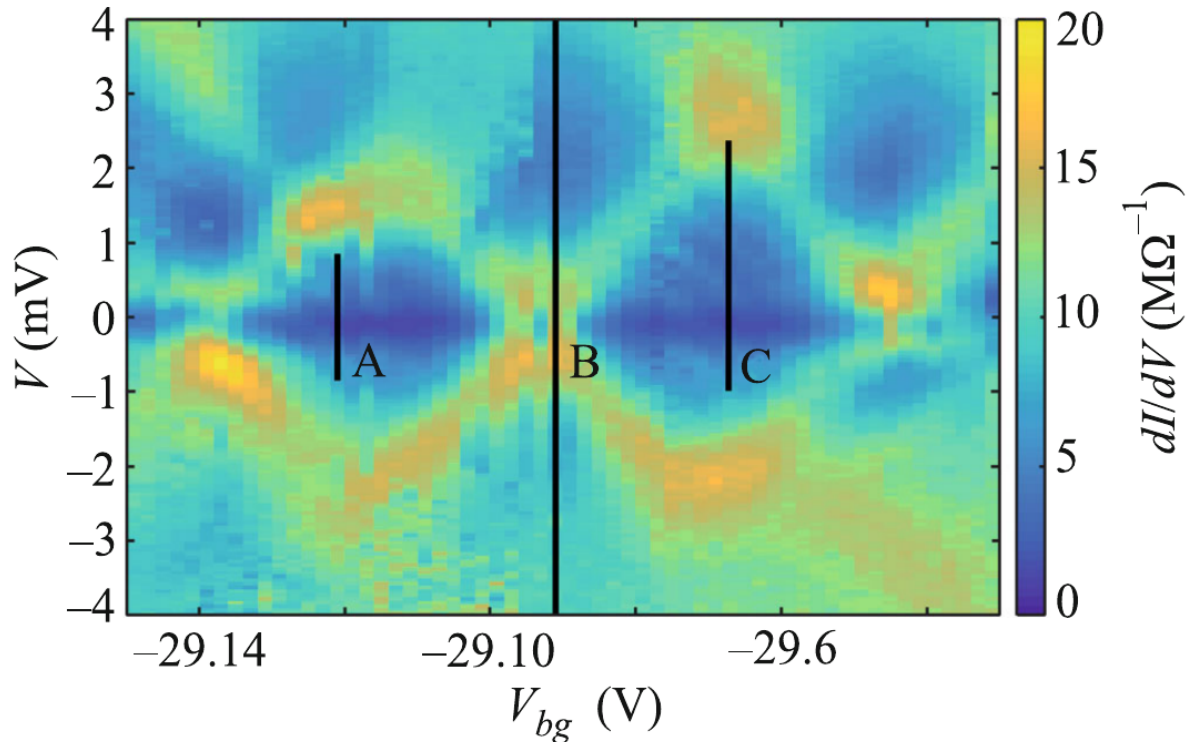
Figure 18. Coulomb diamond measurements. Differential conductance plotted as a function of V_{bg} and bias voltage V. Lines indicate back gate voltage values and bias voltage ranges for which noise measurements were performed.

Diamond-shaped Coulomb blockade is shown in **Figure 18** where inside the diamond's conductance is suppressed. Sequential tunneling is forbidden inside the diamonds and current through the QD exists only due to high-order co-tunneling processes. This device was further utilized for shot-noise measurements and investigation of charge carrier statistics.

4.1.4 Shot Noise

Shot noise in electronic currents originates from the discrete nature of charge carriers[79]. Its observation requires low temperatures and high frequencies in order to differentiate it from the Nyquist-Johnson noise (which is temperature dependent) and flicker noise (1/f noise, which is frequency

dependent). Often the results of shot-noise measurements are presented in the form of the Fano Factor comparison. Fano factor is a ratio of the noise spectral density to the spectra density of a noise with Poissonian statistics. As an example, a diffusive metallic conductor has a Fano factor $F = \frac{1}{3}$ as far as the transmission eigenvalues distribution is universal, in other words the conductance is independent of the shape and length.
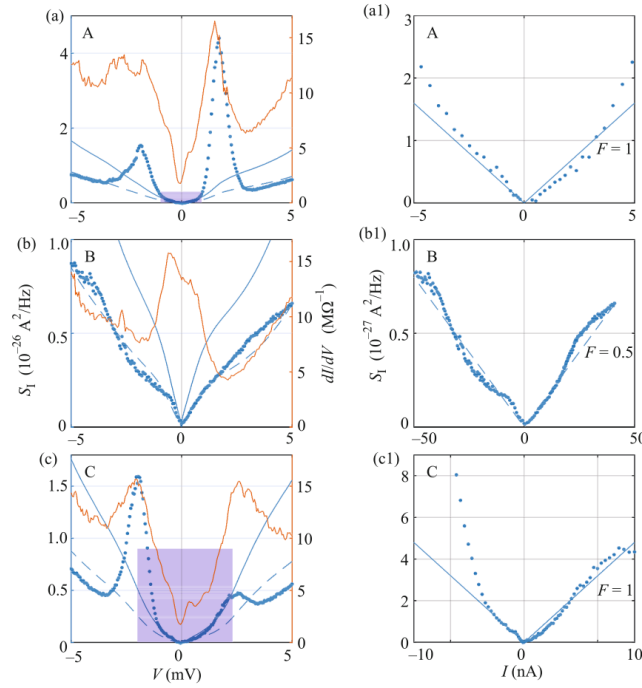

Figure 19. Shot Noise measurements in CB regime. Differential conductance plotted as a function of V_{bg} and bias voltage V. Lines indicate back gate voltage values and current ranges for which noise measurements were performed. Blue dots indicate current noise spectral density S_I, differential conductance dI/dV is indicated by orange lines (corresponding axis are colored respectively). A,B and C indicate the cuts from **Figure 18**. Left columns are plotted versus source-drain voltage, while right panels are plotted versus I, and the region of plot is indicated by shaded region in the corresponding panel on the left (when applicable). Solid blue lines correspond to F =1, dashed lines to F = 0.5

Quantum charge transfer in SWCNT devices is reported in Paper 4[80]. Briefly, three different scenarios are observed in the shot noise dependence. First, when small currents are applied and measurements are performed well inside the Coulomb diamonds (**Figure 19 A** and **C**) the Fano factor is close to 1, i.e. the noise density is approximately $S_I \sim 2eI$. It is rather expected behavior - a shot noise of an

elastic co-tunneling process during which the quantum dot remains in the ground state. The second, distinct scenario is observed when the Fermi level is shifted to the Coulomb resonance point (**panels b and b1**). Here the Fano factor is almost twice smaller. The observation of $0.5 \leq F \leq 1$ is a signature of sequential tunneling in which transport through the QD occurs via two independent tunneling processes across the QD lead barriers. Similar to the non-interacting double-barrier case, this effect is a consequence of current conservation and $F \approx 0.5$ indicates that QD-lead barriers are nearly identical. There are also some regions, where F lies in the range of $[0.3,0.5]$ which is hard to interpret for this particular system. It should be noted that under these conditions (low current values, and V_{bg} region where the SWCNT resistance is lower than 100 kOhm) the clear Coulomb diamond structure was not observed as well. The last, and most striking observation is a super-Poissonian regime with $F \sim 8$ at certain values of V_{bg} near V $\sim$ +- 2mV. In general, such a behavior can be explained by modulation of the current in QD, resulting from the very fast random switching between different quantum states in the regime of Coulomb Blockade. However, low quality of the coulomb diamonds precludes from unequivocal identification of the microscopic states participating in the switching process. Giant noise is therefore a pure interaction effect.

4.2 Graphene

4.2.1 Electronic Band Structure
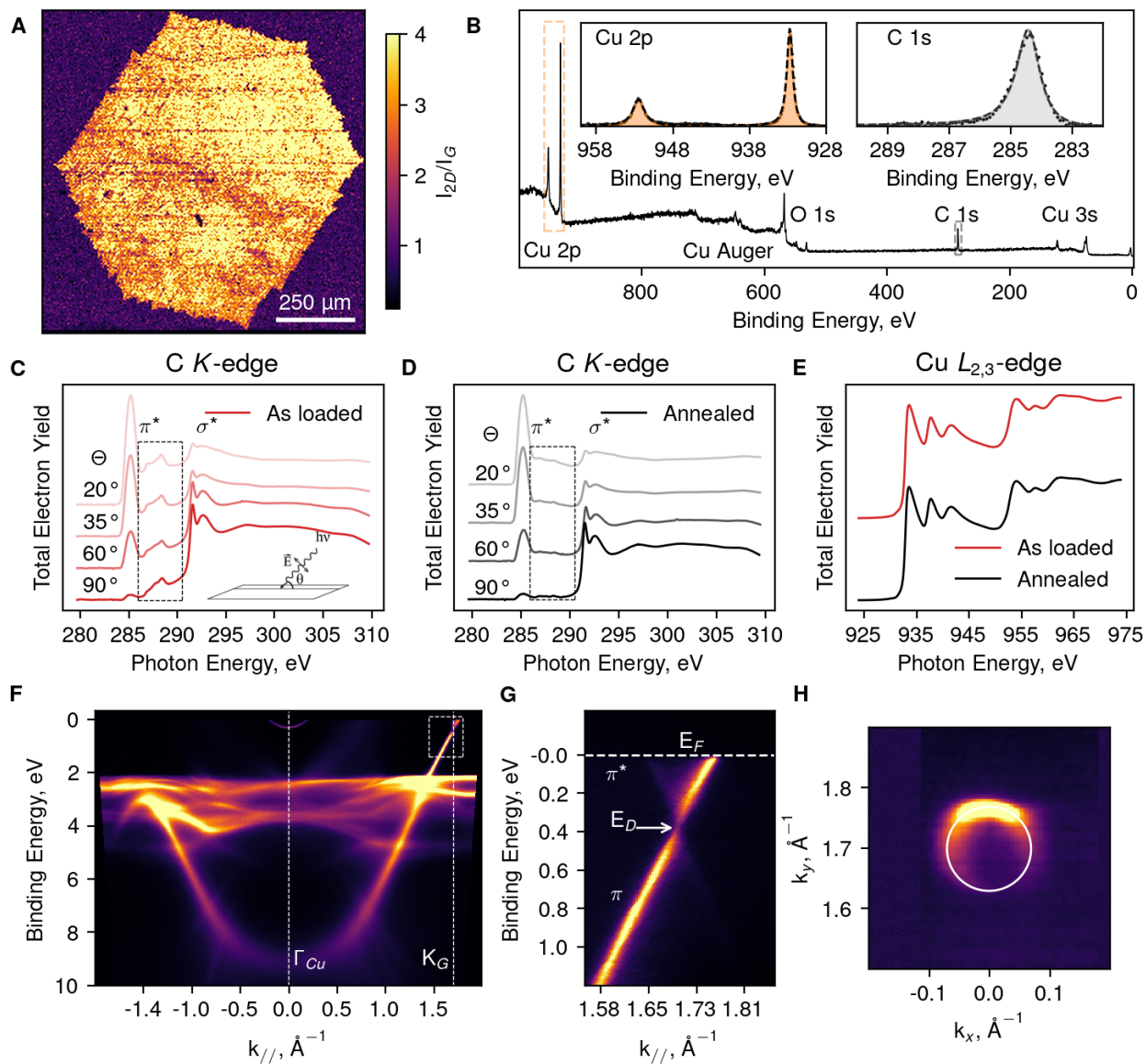
Figure 20. Electronic properties of carbon monoxide derived graphene. (A) Raman spectroscopy map indicating the distribution of I_{2D}/I_G ratio over a mm-size individual single-crystal grain. **(B)** Wide XPS spectra with core-level Cu 2p and C 1s indicated in insets. **(C)-(D) -** NEXAFS spectra for C-K edge and Cu-$L_{2,3}$ edge captured before and after annealing and for various incident angles. **(E-G)** ARPES data showing the band structure of graphene-copper system and Fermi surface of graphene (**H**).

One of the most established techniques for graphene characterization is Raman spectroscopy with a 532 nm laser[81]. The ratio between I_{2D} and I_G may be used to estimate the amount of layers in the system. We have performed Raman spectroscopy mapping over the whole area of the individual mm-size grain and it occured that in each point of scan the aforementioned ratio is larger than 3, which suggests high degree of single-layer nature of the synthesized material (**Figure 20A**). To further analyze the sample we performed X-ray photoelectron spectroscopy investigation of a graphene-copper sample and found out that C 1s line supports sp2 carbon formation similar to non-interacting free-standing graphene[35] (**Figure 20B**). Cu 2p line is also indicative for reduced pure copper substrate[82]. We were unable to perform the annealing procedure of the sample in the XPS preparation chamber and we still observed a weak contribution of oxygen in form of O 1s line, which as we supposed originated from the atmospheric contaminants. To prove it we performed near-edge X-ray absorption fine structure spectroscopy (NEXAFS) utilizing Bessy-II beamline, that revealed extremely pure interface between copper and graphene as all contamination traces[83,84] detected in C-K edge signal were removed by a 300 ℃ annealing procedure. At the same time the copper signal remained unchanged during such treatment and resemble[83] the signal from reduced Cu[083] (**Figure 20 C-D**). Further investigation has been performed with the help of angle-resolved photoelectron spectroscopy (ARPES) that allowed us to analyze the Brilloine zone of copper-graphene samples.

It should be noted that aside from clearly observed d-bands of Cu (**Figure 20E**) and slightly shifted (due to doping) graphene Dirac cone[85] (**Figure 20E-F**) a small parabolic feature is observed in a Γ-point near the Fermi level[86]. This feature originates from the surface states of copper. They are slightly shifted due to the presence of graphene and earlier were observed only in two cases: 1) when a single crystal copper was clean in the UHV chamber of the ARPES device and 2) when a graphene was grown on the surface of a single crystal copper substrate.

Analysis of the Fermi surface delivers the electron effective mass to be of an order of 1.8e-3 m_e which can be used further to estimate the mobility from THz spectroscopy measurements.

4.2.2 Broadband Spectroscopy

Broadband spectroscopy of graphene is a highly informative and non-invasive way to analyze charge transfer properties, which has been already demonstrated for the case of SWCNT films.

UV-vis-NIR region can be utilized as a "consistency test" - monolayer graphene has a plasmon feature located at ~270 nm and 2.3 % absorption of the light with wavelength larger than ~600 nm. In contrast to SWCNTs it does not have features of van Hove singularities. Typical spectrum in this range is shown in **Figure 21a**. It has been captured from the carbon monoxide derived graphene transferred to UV-transparent quartz substrate by a parafilm assisted graphene transfer technique[61]. Concerning the case of MIR-FIR-THz ranges, only the region of k< 500 cm^{-1} holds valuable information on the graphene system as can be seen from **Figure 21b**. As far as various processes, like interference, occur often at these wavelengths, it is impossible to simply subtract the spectrum of the substrate that holds the graphene layer[21]. That's why we firstly transferred a graphene layer on the surface of a parafilm 134 um thick film, measured its spectra and afterwards removed graphene by means of oxygen plasma. After removal of graphene we repeated measurements of transmission coefficient spectra. We have modeled each layer and were able to determine Drude parameters from these spectra. It is important to note that there was a spectra feature in the region of 10-80 cm^{-1} which is often observed during investigation of graphene samples, but, nevertheless, can not be that easily interpreted. It might be associated with cracks formed in the graphene during the transfer procedure, or with defect and doping centers caused again by the etchant. More details can be found in **Paper 1**[36].
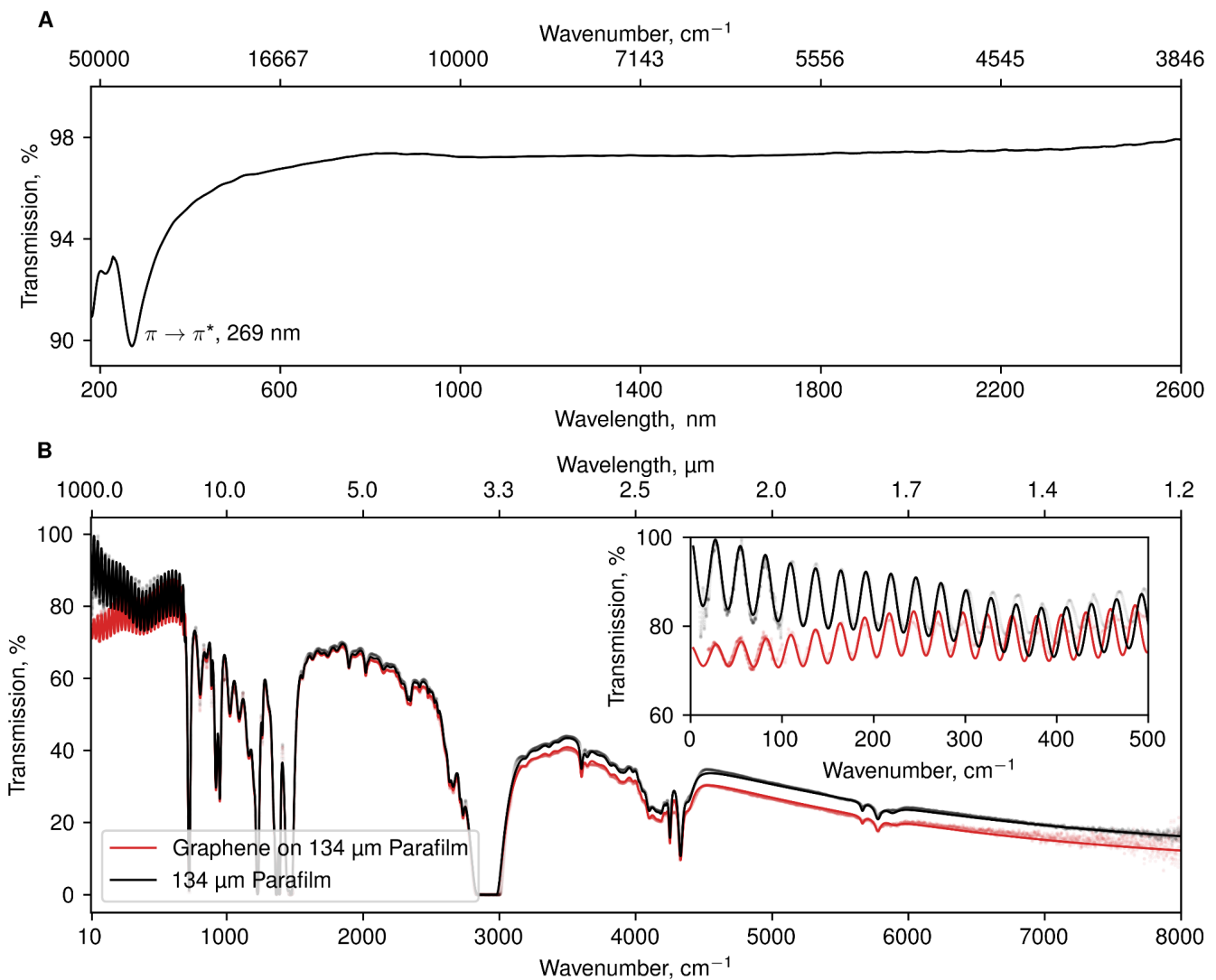
Figure 21. (a), UV-vis-NIR spectrum of the graphene sample transferred to the quartz substrate. **(b),** NIR-MIR-FIR-THz spectrum of the graphene on the 134 μm thick parafilm substrate. Deep minima above ≈500 cm^{-1} are due to molecular vibrations in parafilm substrate.In the inset, the region of interest is illustrated, where the presence of free charge carriers in graphene influences the transmissivity.

Comparing THz spectroscopy of SWCNT films and graphene we should note that in this case the most effect is also defined by delocalized free charge carriers illustrated by Drude-like contributions.
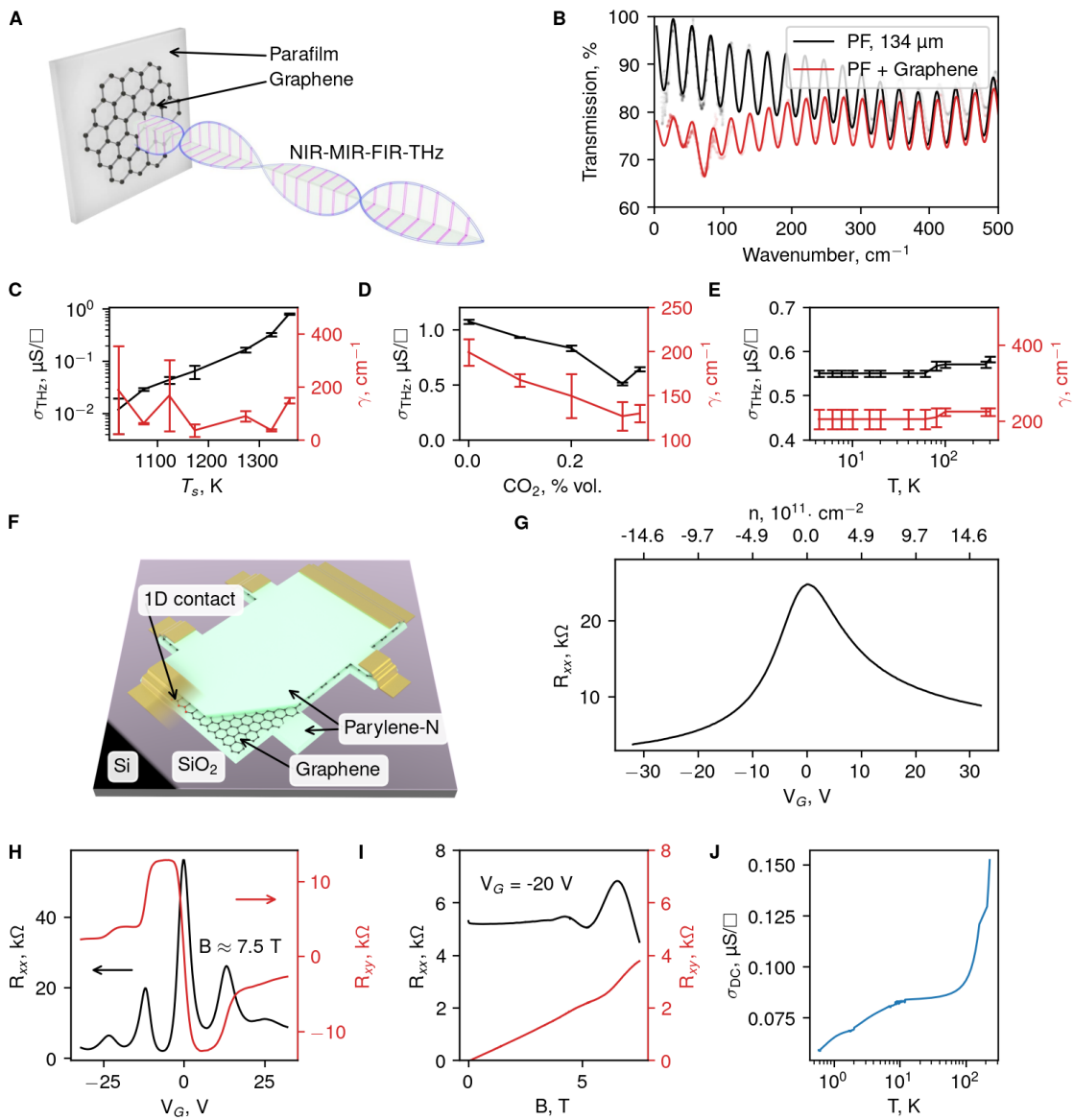
Figure 22. Charge transfer measurements in graphene devices. (A-E) THz spectroscopy data summary for investigation of the crystallite-size influence on the transmission coefficient spectra. **(F)** Schematic illustration of the Hall-bar structure of graphene encapsulated in Parylene-N. Side contacts are fabricated with the help of optical lithography, oxygen plasma etching and thermal deposition of metals (Cr/Au). **(G)** Transconductance of 0.5x0.3 mm device fabricated from individual graphene single crystal captured at ambient conditions. **(H-E)** Longitudinal and transverse resistance of a Hall-bar structure measured at 0.5 K in the presence of strong magnetic field showing typical behavior of quantum hall effect. The second graph shows the dependence of these two resistances on the magnetic field at a fixed back-gate voltage. **(F)** Temperature dependence of the conductivity.

We have observed some narrow resonance-like absorption lines that can be attributed to various plasmonic oscillations caused by cracks and wrinkles in graphene film. Apart from SWCNTs no peculiar contributions to the spectra exist at 10 cm^{-1} and below. It is interesting that technically Parylene-N is also transparent in THz-FIR range and can be used in order to make flexible field-effect transistors with graphene channel and graphene gate-electrode for more informative analysis. Assumptions made from the scattering rate factor $Y \sim 90\text{-}110$ cm^{-1} and ARPES measurements allow us to estimate the mobility of graphene in this case at roughly 10000 cm^{2}V^{-1}s^{-1}, which is larger than the one obtained from FETs measured in DC-regime. That can be explained by the fact that by the moment of graphene transfer to parafilm film, the latter was applied in a liquid form to the surface of the sample and the catalyst was simply removed. Due to utilization of molten copper substrate, the final sample's surface is far from being flat. It results in generation of additional cracks and wrinkles during transfer procedure from parafilm to the target parylene-N coated Si wafer. The second reason for such discrepancy originates from the fact that effective mass determined from ARPES measurements of the Fermi surface is obtained in UHV conditions, while THz spectra were collected at regular HV conditions of roughly 2x10^{-6} mbar. THz mobility often claimed to be an overestimate value, as well as FET ones. Nevertheless, due to the fact that graphene transfer procedure is still a bottleneck part of industrial graphene production it is important to at least estimate the electronic properties of intact, unperturbed graphene. As also seen from the dependence of the Drude parameters on the synthesis parameters (synthesis Temperature, **Figure 22C**, and CO$_2$ content, **Figure 22D**) we can conclude that higher temperatures and higher CO$_2$ content result in larger crystals forming polycrystalline film. More detail on graphene mobility analysis is presented in the next subsection and **paper 1**.

4.2.3 Quantum Hall Effect

Firstly we measured such graphene hall-bar structures in the Field Effect Transistor fashion and the hallmark gate trace is shown in **Figure 22G**. Mobility values extracted from these data fall in the range of 1500-4000 cm^{2}V^{-1}s^{-1}. Further we subjected our samples to high magnetic fields to detect Quantum Hall Effect phenomena - feature specific for 2D electron gasses. We were limited to roughly 8 T and did not manage to observe clearly plateaus and zeroing of the longitudinal resistance, but all characteristic features in the density of state plots can be observed (see **Figure 22H-J**)

Chapter 5. Atomic Force Microscopy Lithography for SWCNT Films

Based on the investigated properties of the carbon nanotubes, further research efforts were done to find a way to manipulate its optical properties on the nanoscale. We have observed that mechanical and optical properties of SWCNT films largely depend on their density, which so far can be changed with the help of either tension forces resulting from liquid drop evaporation from the film (liquid-driven densification[87]) or with the help of mechanical indentations[88]. We have begun this research branch modeling of the SWCNT film mechanical behavior taking into account detailed geometry of the films.

5.1 Densification Model

SWCNT film mechanical model is described in detail in Drozdov et al[24] and was applied to simulate the densification process often utilized to improve opto-electronic properties of the SWCNT films. We have begun investigation with a simple liquid-driven densification, when a drop of a solvent (e.g. water) is placed onto the film and due to the surface tension and solvent evaporation the film gets denser. Experimental observations were completely consistent with the results of modeling, while computer generated data resulted in a deeper understanding of the physical processes occurring at the micro- and nanoscale. These details are almost inaccessible from the experimental point of view. For computer generated samples we have employed Mesoscopic Distinct Element Modeling (MDEM)[89,90].

In our first paper[24], we were comparing the calculations of liquid-driven densification with experimental observations made with the help of Scanning Electron Microscopy and Transmission Electron Microscopy. Further we utilized these models to explain local ultra-densification performed with the help of an AFM tip. Experimental data collected for the verification of MDEM is summarized in **Figure 23**.
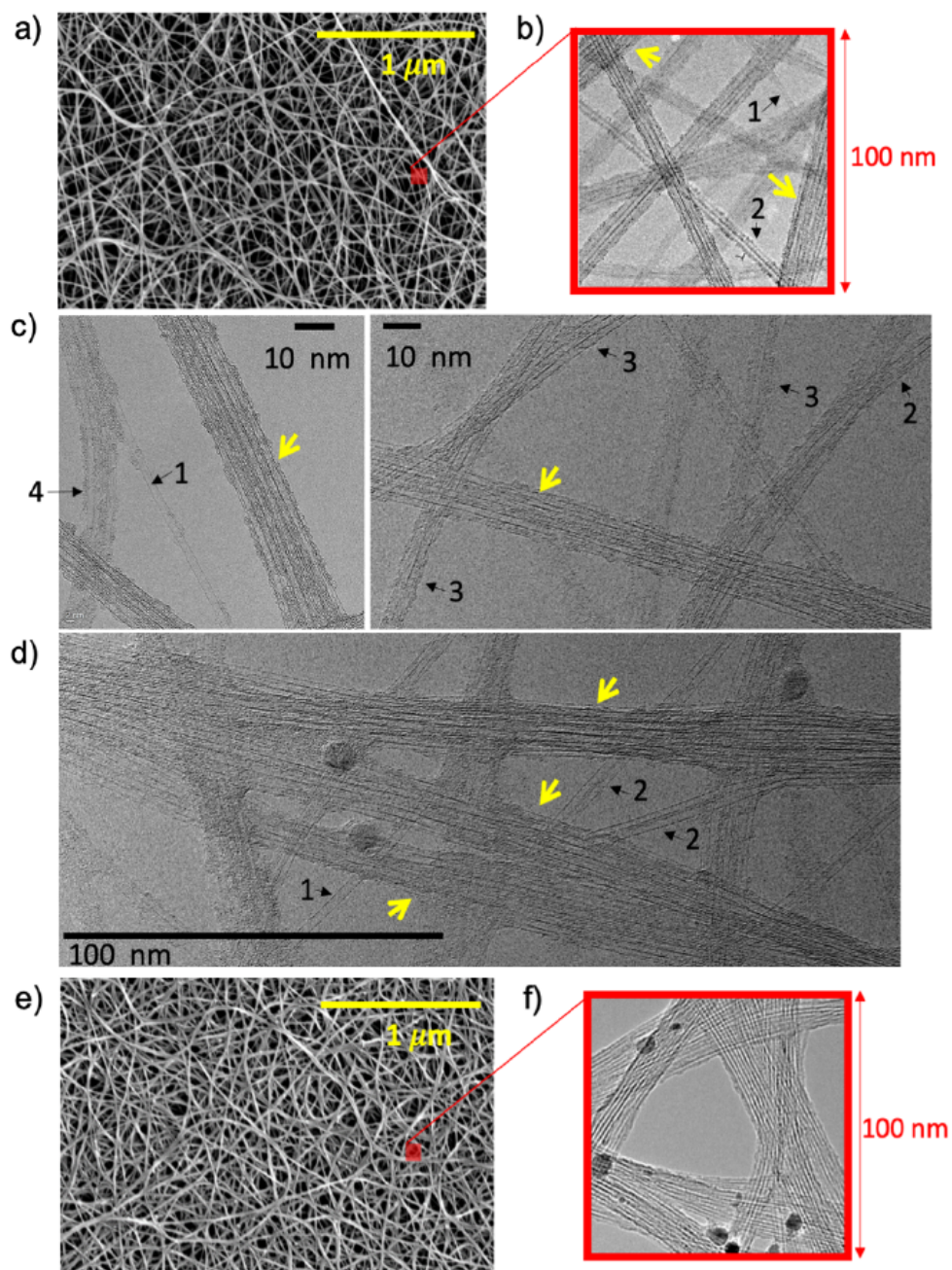
Figure 23. Multiscale structure of the pristine (a)–(d) and densified **(e)–(f)** SWCNT film: **(a)** SEM showing an entangled structure of μm-long wavy bundles. **(b)** TEM of individual and 2-CNT bundles coexisting with "medium" ~10 nm diameter bundles (indicated with yellow arrow heads) on a 100 nm scale. TEM detailing **(c)** ~10 nm diameter bundles and **(d)** their merging into a thicker "large" bundle. Individual and 2–3 CNT bundles (indicated by black arrows) can be still observed. **(e)** SEM showing μm-long wavy bundles. **(f)** TEM of few-CNT bundles zipped on a 100 nm scale.

5.2 Local Ultra-Densification Approach

Local ultra-densification is a process when AFM is used in a lithographic mode[91] to locally change mechanical density of the SWCNT film. This process can not be done in a classical contact mode, when the tip is constantly pinned to the surface of the sample. Lateral movement will be destructive in this case and can not result in a clear pattern formed on the sample's surface. On the contrary, tapping mode can be used for such a procedure in a hard tapping regime, when the feedback is tuned so that auto-generation begins. In this case, the tip hits the surface of the sample, but laterally moves in the retracted state.

However, it is rather hard to quantify important technological parameters in this case, and assign them in a simple way with the desired final optical parameter. Therefore we have mostly utilized AFMs that are capable to operate in a "sewing machine" regime, i.e. PeakForce tapping in Bruker Multimode V8 and Hybrid Mode in NTM-DT Integra. At each point of scan the tip is brought into contact at a desired force value, while in lateral direction the tip moves in a retracted state, and at each point of scanning the complete force-distance curve is captured. Regular AFM tips that withstand this procedure have a radius of 20-30 nm, and tip's pyramide angle of 25°, which determines the resolution roughly at 100 nm for 300 nm thick film. It should be noted that this parameter is sample dependent, as the SWCNT film thickness largely influences the patterning outcome.

Potentially, such an issue can be minimized by utilization of rod-like tips, which are not yet widely produced. It is extremely hard to investigate the individual indentation process performed by the tip due to the fact that its size is comparable to the tip. In order to have an adequate picture of the process we did Helium Ion Microscopy, which delivered state-of-the art resolution and material contrast allowing visualization of the individual tubes and bundles with great precision. Furthermore our colleagues from the University of Minneapolis (USA) and Twente University (Netherlands) performed careful MDEM simulations of the tip-sample interaction. Such modeling allowed us to understand typical changes occurring at the nanoscale and is an excellent way to visualize the densification process. These data are shown in **Figure 24**. As model film we utilized roughly 135 nm (h_0) relaxed swcnt film, which was densified by an indenter to a instantaneous height value h_m of roughyl 20 nm. After the indenter was removed, the film relaxed to a height h of approximatelly 35 nm and the overall thickness was reduced to 100 nm outside of the densified region.
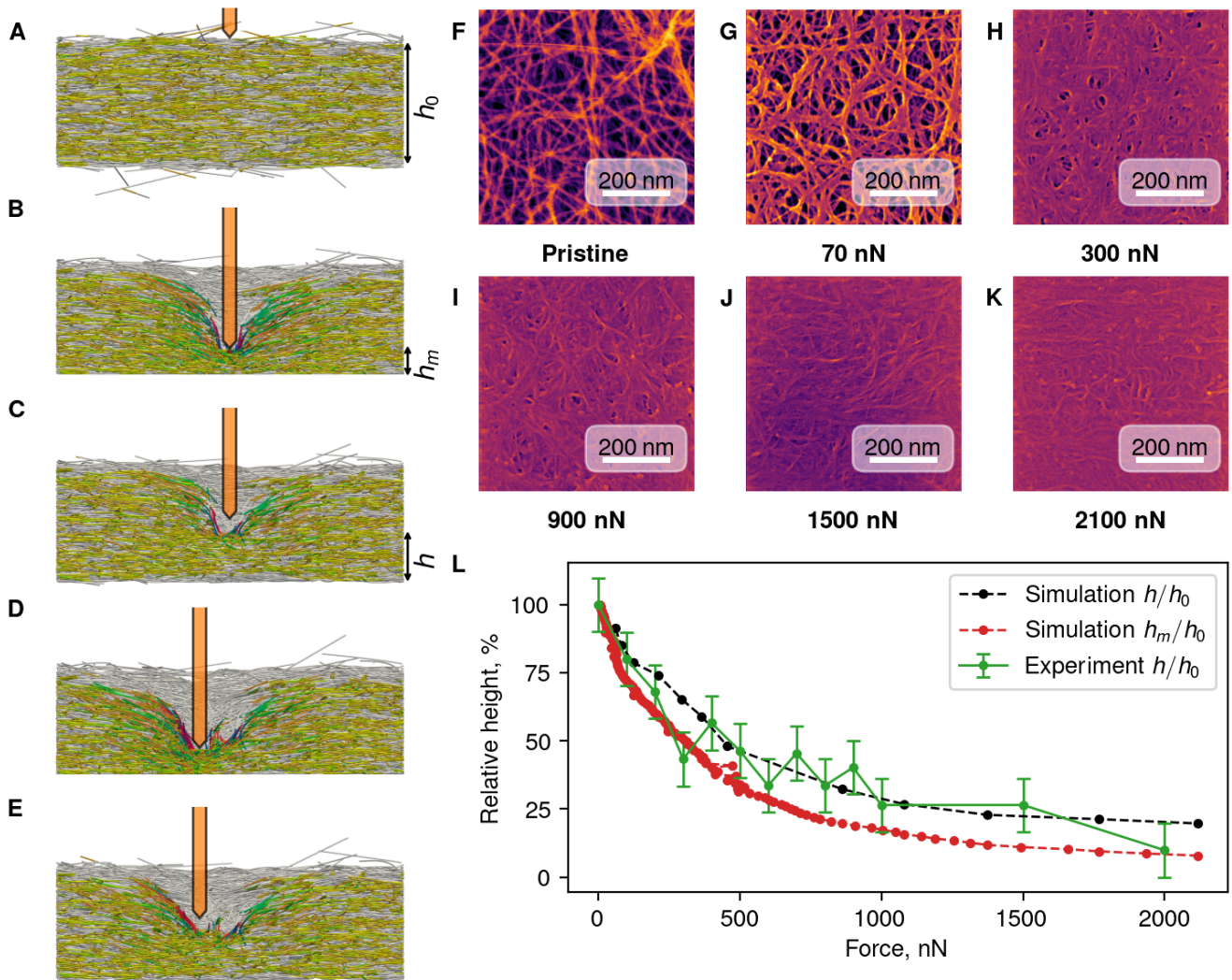
**Figure 24. Local ultradensification of the SWCNT film.** (**A-E**) A step-by-step MDEM simulation of the local tip-driven densification process. (**F-K**) HeIM images of the AFM-densified regions, densification force of the calibrated tip is indicated under each panel. (**L**) Relative height dependence on the indentation force value. Experimental data are compared to both compression and relaxed simulation values.

5.3 Optically Active Devices

It turned out that such densification allows precise sub-wavelength modification of the reflection coefficient. Even if the initial SWCNT film is deposited so thick that it neither reflects nor transmits significant amounts of light, ultimately densified regions tend to be highly reflecting in the visible range. Such lithography can be utilized to fabricate various optical devices such as Fresnel lenses, metamaterials and many others directly on the surface of flexible, stretchable and electrically conductive material. Firstly we patterned large reflective squares to show how the reflectance changes during compression and finally came to patterning of static computer-generated holograms and diffraction gratings. Even though these devices had a small efficiency when compared to standard metallic structures, their mechanical properties justify their drawbacks. These results are described in detail in **Paper 3**.

Briefly, the reflection enhancement (RE) of SWCNT film (optical image in **Figure 25A**) is depicted in **Figure 25B** in the form of the map. The increase in the reflectivity is tightly bound to the spectral range and the applied densification force. It has occured that the most prominent effect takes place in the short wavelength region of UV-vis (**Figure 25C**). Maximal reflection enhancement for particular wavelengths are plotted in **Figure 25C**. It is important to note, that the reflection enhancement is naturally bound to the initial pristine film thickness - thin films can not be densified into reflective surface keeping its sparse network form (see **Figure 25D**). Scattering reduction due to the densification seems to play a major role in the RE phenomena as a part of an overall absorption reduction (see **Figure 25E**).
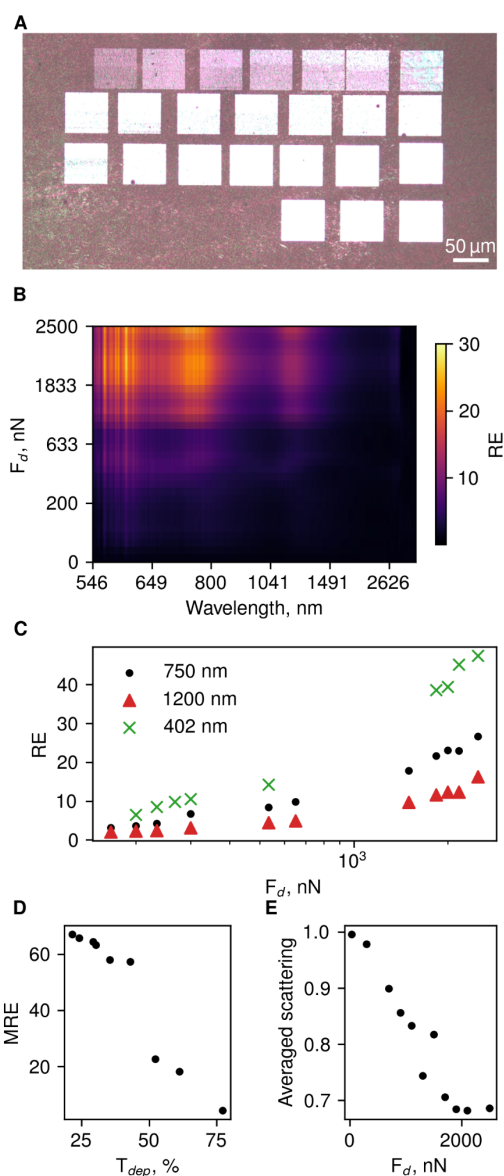
Figure 25. Optical properties controlled by local densification. (**A**) Optical microscope photo of the densified squares in SWCNT film taken in the reflected light. Densification force values (PeakForce tapping) growth from left to right and from top to bottom gradually from 33 nN up to 2500 nN (**B**) Reflection enhancement map illustrating the dependence of RE on the densification force (PeakForce tapping) and wavelength. (**C**) Dependence of the reflection enhancement value normalized to the reflection of pristine film for UV (402 nm), vis (750 nm) and NIR (1200 nm) wavelengths for a fixed thickness of the SWCNT film at ~ 250 nm (T600 = 40-50 %). (**D**) Maximal Reflection Enhancement (MRE) for samples densified at 2500 nN of the different initial thicknesses (T600). (**E**) Averaged scattering intensity (relative to the pristine film) dependence on the densification force, indicating one source of the reflection enhancement.

Finally we were able to define a computer generated hologram of Sk logo (CGH, shown in **Figure 26 A-E**) and a set of diffraction gratings (shown in **Figure 25F-H**).
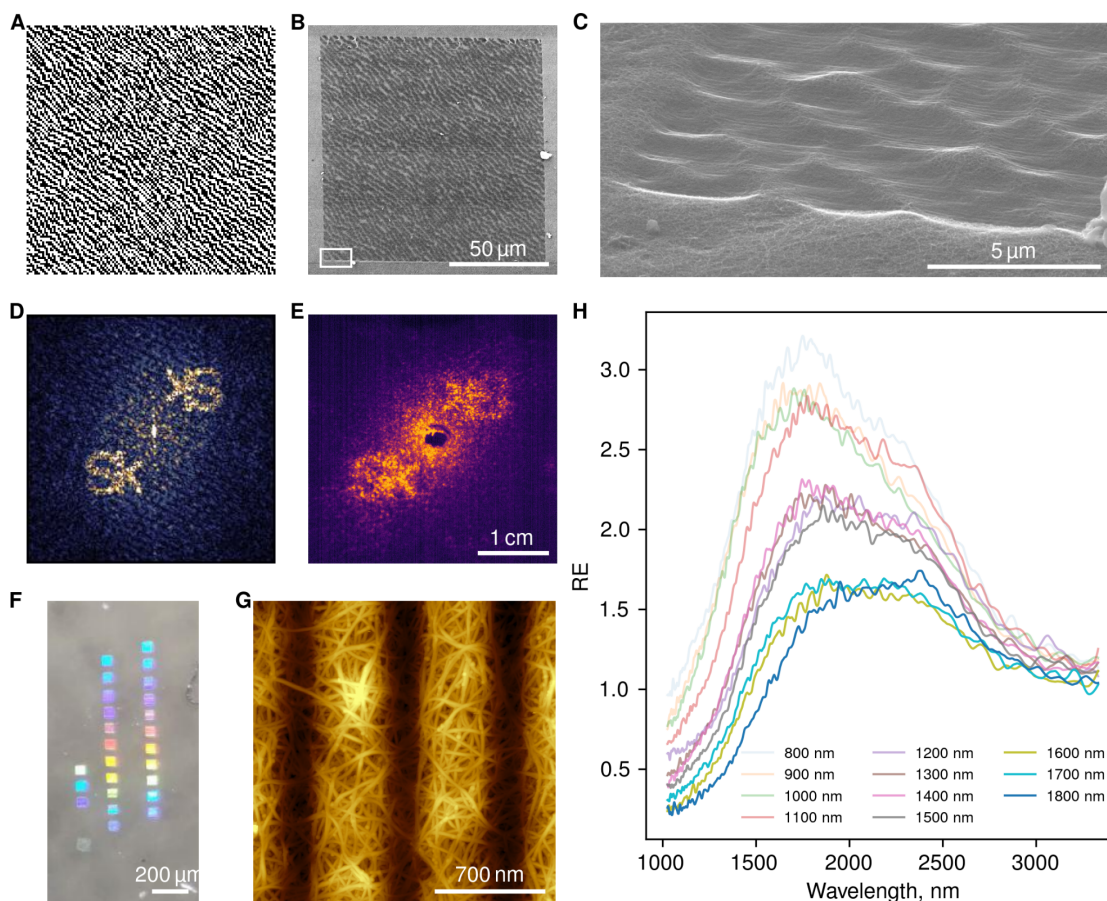
Figure 26. Optically active media defined by means of SPL. **A-E** Static computer-generated hologram patterning in the SWCNT film on a quartz substrate. (**A**) Initial pattern generated by computer. (**B**) An SEM image of the pattern 120x120 μm2 transferred by means of SPL (Hybrid™ mode) and (**C**) close look on the left bottom corner. (**D**) Fourier transform of image (**B**). (**E**) Optical photograph of the hologram recovered by 650 nm laser. (**F**) Optical photograph of a set of diffraction gratings with different periods patterned in SWCNT film on quartz substrate by hard tapping SPL. An AFM (**G**) image of one of the diffraction gratings with 800 nm period. (**H**) NIR spectrum of the reflection enhancement of diffraction gratings indicating spectral features resulting from the pattern. This feature may be assigned to some collective excitations occurring in these gratings.

CGH was calculated by prof. Sergey Zaitsev and Dr. Aleksandr Svintsov at IPTM, RAS. An initial CGH is shown in **Figure 26 A**. Image was transferred to the surface of an SWCNT film by means of

Hybrid Mode AFM lithography. Further it was analyzed by SEM (**Figure 26B** and **C**). To check the correctness we performed Fourier transform of the image **26B** (see **Figure 26D**) and further reconstructed the hologram with the help of laser radiation (**Figure 26 E**).

We also were able to observe spectral features (**Figure 26 H**) in the near-infrared region for diffraction gratings (**Figure 26 F,G**). However, we did not manage to find the explanation for the nature of observed spectral lines.

Chapter 6. Conclusions and Perspectives

To sum up, the key goal of this research has been successfully achieved - carbon monoxide has been utilized for the first time to synthesize graphene. Previous successful realization of aerosol-assisted CVD synthesis of single-walled carbon nanotubes (SWCNT) has formed the basis for graphene reactors. **(1) Ambient pressure (and high pressure as well) CVD reactor designed at Skoltech facilitated single-crystal monolayer graphene grains with up to 5 mm size, limited only by the reactor chamber size.** It is important to mention an unprecedented chemical purity of the synthesized graphene - the purity is comparable to the exfoliated graphene samples. It should be stressed that the observed features, i.e. copper surface states, in the electronic band structure of synthesized graphene-copper composite are also quite unique and manifest extreme purity of the metallic state. Their uniqueness lies in the fact that one requires a perfect copper surface to observe such a state. It should be explicitly noted that these surface states are protected by graphene and can be easily studied by means of other photoelectron spectroscopy techniques, or even employed in practical devices. The next to recall is the peculiar interaction of the carbon source gas with the metallic catalyst, which first ensures monocrystallization of the catalyst and formation of the specific crystal-cut which hides a great potential for real world application of the metal-graphene composite for various catalytic reactions and other surface-dependent processes (e.g. adsorption for gas sensors).

What is more important - this result paves the way for novel tasks and problems. To mention a few - a great potential is hidden towards application of non-catalytic reaction of carbon monoxide with different metals and semiconductors, that possibly may result in the formation of a single graphitic layer. One of such potential techniques relies on the utilization of titanium[69] - carbon monoxide, when interacting with the surface of this metal at elevated temperatures may form a graphitic layer turning the metal underneath to its oxide. So far a transfer-free graphene may be formed - a thin layer of a high-k dielectric (e.g., TiO_2) can be utilized as a gate dielectric and the device may be formed right on the surface of the sample after synthesis. Finally, utilization of the Boudouard reaction largely simplifies the setup which is extremely important for industrial application of the suggested scalable synthesis technique.

Broad-band spectroscopy of carbon monoxide derived CNMs speaks in favor of high quality of the synthesized materials. It was possible to (2) **determine the main contribution of delocalized carriers**

into the spectral behavior for pristine, doped SWCNTs and graphene in the THz range (for the case of graphene it can be also claimed regarding almost the whole spectral range from UV to THz). **(3) Microscopical analysis further helped to understand the contribution of the defects and tunnel junctions into the FIR-THz ranges**. Often it is complicated to associate absorption spectral lines with collective excitations in the system, while these simple examples of graphene and SWCNTs can be further used to understand peculiarities in optical conductivity of other low dimensional materials.

Optical charge transfer investigation was also supported by the study of nano-devices, when individual CNM structure was used as a basis. Typically, we had field-effect transistor geometry with Hall-bar contacts organization when possible. Low temperature experiments and shot-noise measurements allowed us to observe quantum phenomena in individual SWCNT devices. The key finding **(4) is the observation of a super-poissonian shot-noise in the SWCNT quantum dot tuned to the specific regime**, when non-elastic processes and resonant tunneling dominate. For the case of graphene, **successfully encapsulated with the developed parylene-N coating (5)**, we were able to observe a hallmark feature - **(6) quantum hall effect in macroscopically large mm-size samples**.

Finally, **(7) novel patterning techniques were developed taking into account understanding of mechanical and optoelectronic properties of the synthesized materials**. Both atomic force microscopy lithography (AFML) and regular electron-beam lithography (EBL) methods, are highly requested by fastly growing material science and biological communities - such hacks towards compatibility with delicate materials allows a larger set of samples to be investigated and patterned at the nanoscale. It was shown that SWCNT films can be modified by means of AFML, resulting in stretchable and flexible optically active devices. Grayscale lithography technique overcomes limitations of common EBL and OL methods employed before, facilitating creation of metasurfaces on small and curved meshy materials. This technique opens an avenue for further application with various other nanowires and nanotubes of e.g. semiconducting nature. From the other side, gentle patterning techniques, i.e. novel EBL and OL resists that allow operation with mild physical and chemical treatment of the target material surface, are reviewed and developed.

Bibliography

1. A two-dimensional outlook. *Nat. Electron.* **4**, 767–767 (2021).

2. Berdyugin, A. I. *et al.* Out-of-equilibrium criticalities in graphene superlattices. *Science* (2022) doi:10.1126/science.abi8627.

3. Novoselov, K. S. *et al.* Electric Field Effect in Atomically Thin Carbon Films. *Science* **306**, 666–669 (2004).

4. Sun, L. *et al.* Chemical vapour deposition. *Nat. Rev. Methods Primer* **1**, 1–20 (2021).

5. Bronikowski, M. J., Willis, P. A., Colbert, D. T., Smith, K. A. & Smalley, R. E. Gas-phase production of carbon single-walled nanotubes from carbon monoxide via the HiPco process: A parametric study. *J. Vac. Sci. Technol. A* **19**, 1800–1805 (2001).

6. Iakovlev, V. Ya. *et al.* Fine-tuning of spark-discharge aerosol CVD reactor for single-walled carbon nanotube growth: The role of ex situ nucleation. *Chem. Eng. J.* **383**, 123073 (2020).

7. Kaskela, A. *et al.* Aerosol-Synthesized SWCNT Networks with Tunable Conductivity and Transparency by a Dry Transfer Technique. *Nano Lett.* **10**, 4349–4355 (2010).

8. Krasnikov, D. V. *et al.* A spark discharge generator for scalable aerosol CVD synthesis of single-walled carbon nanotubes with tailored characteristics. *Chem. Eng. J.* **372**, 462–470 (2019).

9. Xu, S., Zhang, L., Wang, B. & Ruoff, R. S. Chemical vapor deposition of graphene on thin-metal films. *Cell Rep. Phys. Sci.* **2**, 100372 (2021).

10. Machac, P., Cichon, S., Lapcak, L. & Fekete, L. Graphene prepared by chemical

vapour deposition process. *Graphene Technol.* **5**, 9–17 (2020).

11.   Farjadian, F. *et al.* Recent Developments in Graphene and Graphene Oxide: Properties, Synthesis, and Modifications: A Review. *ChemistrySelect* **5**, 10200–10219 (2020).

12.   Sun, B. *et al.* Synthesis of Wafer-Scale Graphene with Chemical Vapor Deposition for Electronic Device Applications. *Adv. Mater. Technol.* **6**, 2000744 (2021).

13.   Kim, S. H. *et al.* Fast synthesis of large-scale single-crystal graphene with well-defined edges upon sodium chloride addition. *Carbon* **158**, 904–911 (2020).

14.   Moisala, A., Nasibulin, A. G. & Kauppinen, E. I. The role of metal nanoparticles in the catalytic production of single-walled carbon nanotubes—a review. *J. Phys. Condens. Matter* **15**, S3011–S3035 (2003).

15.   Moisala, A. *et al.* Single-walled carbon nanotube synthesis using ferrocene and iron pentacarbonyl in a laminar flow reactor. *Chem. Eng. Sci.* **61**, 4393–4402 (2006).

16.   Deitz, V. R. & Prosen, E. J. Reaction of Carbon Monoxide with Graphitic Carbon at 450° C. *Nature* **181**, 109–110 (1958).

17.   Bond, R. L. & Pinchin, F. J. Formation of Carbon by Decomposition of Carbon Suboxide at 750-780° C. *Nature* **182**, 129–129 (1958).

18.   Baird, T., Fryer, J. R. & Grant, B. Carbon formation on iron and nickel foils by hydrocarbon pyrolysis—reactions at 700°C. *Carbon* **12**, 591–602 (1974).

19.   Trimm, D. L. The Formation and Removal of Coke from Nickel Catalyst. *Catal.*

Rev. **16**, 155–189 (1977).

20. Cao, Q., Tersoff, J., Farmer, D. B., Zhu, Y. & Han, S.-J. Carbon nanotube transistors scaled to a 40-nanometer footprint. *Science* **356**, 1369–1372 (2017).

21. Born, M. Principles of Optics - 6th Edition. https://www.elsevier.com/books/principles-of-optics/born/978-0-08-026482-0.

22. Moreau, W. M. Positive Radiation Resists. in *Semiconductor Lithography: Principles, Practices, and Materials* (ed. Moreau, W. M.) 81–155 (Springer US, 1988). doi:10.1007/978-1-4613-0885-0_3.

23. Chiu, G. L.-T. & Shaw, J. M. Optical lithography: Introduction. *IBM J. Res. Dev.* **41**, 3–6 (1997).

24. Drozdov, G. *et al.* Densification of single-walled carbon nanotube films: Mesoscopic distinct element method simulations and experimental validation. *J. Appl. Phys.* **128**, 184701 (2020).

25. Garcia, R., Knoll, A. W. & Riedo, E. Advanced scanning probe lithography. *Nat. Nanotechnol.* **9**, 577–587 (2014).

26. Grebenko, A. *et al.* Green Lithography for Delicate Materials. *Adv. Funct. Mater.* **31**, 2101533 (2021).

27. Iijima, S. & Ichihashi, T. Single-shell carbon nanotubes of 1-nm diameter. *Nature* **363**, 603–605 (1993).

28. Novoselov, K. S. *et al.* Two-dimensional gas of massless Dirac fermions in graphene. *Nature* **438**, 197–200 (2005).

29.   Novoselov, K. S. *et al.* A roadmap for graphene. *Nature* **490**, 192–200 (2012).

30.   Zhang, Y., Tan, Y.-W., Stormer, H. L. & Kim, P. Experimental observation of the quantum Hall effect and Berry's phase in graphene. *Nature* **438**, 201–204 (2005).

31.   Wang, M. *et al.* Single-crystal, large-area, fold-free monolayer graphene. *Nature* **596**, 519–524 (2021).

32.   Li, X. *et al.* Large-Area Graphene Single Crystals Grown by Low-Pressure Chemical Vapor Deposition of Methane on Copper. *J. Am. Chem. Soc.* **133**, 2816–2819 (2011).

33.   Monachino, E. *et al.* Reactivity of Carbon Dioxide on Nickel: Role of CO in the Competing Interplay between Oxygen and Graphene. *J. Phys. Chem. Lett.* **5**, 1929–1934 (2014).

34.   Liu, Y. *et al.* Giant enhancement in vertical conductivity of stacked CVD graphene sheets by self-assembled molecular layers. *Nat. Commun.* **5**, 5461 (2014).

35.   Kovtun, A. *et al.* Accurate chemical analysis of oxygenated graphene-based materials using X-ray photoelectron spectroscopy. *Carbon* **143**, 268–275 (2019).

36.   Grebenko, A. K. *et al.* High-Quality Graphene Using Boudouard Reaction. *Adv. Sci.* **n/a**, 2200217.

37.   Schindele, J., Baumgartner, A. & Schönenberger, C. Near-Unity Cooper Pair Splitting Efficiency. *Phys. Rev. Lett.* **109**, 157002 (2012).

38.   Cao, Q. *et al.* End-bonded contacts for carbon nanotube transistors with low, size-independent resistance. *Science* **350**, 68–72 (2015).

39.   Jiang, S. *et al.* Ultrahigh-performance transparent conductive films of carbon-welded isolated single-wall carbon nanotubes. *Sci. Adv.* **4**, eaap9264 (2018).

40.   Zhang, D. *et al.* Transparent, Conductive, and Flexible Carbon Nanotube Films and Their Application in Organic Light-Emitting Diodes. *Nano Lett.* **6**, 1880–1886 (2006).

41.   Li, H. *et al.* Electrode-Free Anodic Oxidation Nanolithography of Low-Dimensional Materials. *Nano Lett.* **18**, 8011–8015 (2018).

42.   Gan, T., Wu, B., Zhou, X. & Zhang, G. Ultrahigh resolution, serial fabrication of three dimensionally-patterned protein nanostructures by liquid-mediated non-contact scanning probe lithography. *RSC Adv.* **6**, 50331–50335 (2016).

43.   Liu, Y. *et al.* Promises and prospects of two-dimensional transistors. *Nature* **591**, 43–53 (2021).

44.   Kambe, T. *et al.* π-Conjugated Nickel Bis(dithiolene) Complex Nanosheet. *J. Am. Chem. Soc.* **135**, 2462–2465 (2013).

45.   Wang, Z. F., Liu, Z. & Liu, F. Organic topological insulators in organometallic lattices. *Nat. Commun.* **4**, 1471 (2013).

46.   Takenaka, T. *et al.* Strongly correlated superconductivity in a copper-based metal-organic framework with a perfect kagome lattice. *Sci. Adv.* **7**, eabf3996.

47.   Podzorov, V. Organic single crystals: Addressing the fundamentals of organic electronics. *MRS Bull.* **38**, 15–24 (2013).

48.   Choi, H. H., Cho, K., Frisbie, C. D., Sirringhaus, H. & Podzorov, V. Critical

assessment of charge mobility extraction in FETs. *Nat. Mater.* **17**, 2–7 (2018).

49.　Choi, H. H. *et al.* Hall Effect in Polycrystalline Organic Semiconductors: The Effect of Grain Boundaries. *Adv. Funct. Mater.* **30**, 1903617 (2020).

50.　Fusella, M. A. *et al.* Use of an Underlayer for Large Area Crystallization of Rubrene Thin Films. *Chem. Mater.* **29**, 6666–6673 (2017).

51.　Grebenko, A. *et al.* Impedance spectroscopy of single bacterial nanofilament reveals water-mediated charge transfer. *PLOS ONE* **13**, e0191289 (2018).

52.　Gorby, Y. A. *et al.* Electrically conductive bacterial nanowires produced by Shewanella oneidensis strain MR-1 and other microorganisms. *Proc. Natl. Acad. Sci.* **103**, 11358–11363 (2006).

53.　Lovley, D. R. & Walker, D. J. F. Geobacter Protein Nanowires. *Front. Microbiol.* **10**, 2078 (2019).

54.　Mostert, A. B. *et al.* Role of semiconductivity and ion transport in the electrical conduction of melanin. *Proc. Natl. Acad. Sci.* **109**, 8943–8947 (2012).

55.　Grebenko, A. K., Motovilov, K. A., Bubis, A. V. & Nasibulin, A. G. Gentle patterning approaches towards compatibility with bio-organic materials and their environmental aspects. *ArXiv220208667 Cond-Mat Physicsphysics* (2022).

56.　Erdmann, A. *Optical and EUV lithography: a modeling perspective*. (SPIE--The International Society for Optical Engineering, 2021).

57.　Guo, L. J. Recent progress in nanoimprint technology and its applications. *J. Phys. Appl. Phys.* **37**, R123–R141 (2004).

58.   Huo, F. *et al.* Beam pen lithography. *Nat. Nanotechnol.* **5**, 637–640 (2010).

59.   Guo, H. *et al.* Insulating SiO2 under Centimeter-Scale, Single-Crystal Graphene

        Enables Electronic-Device Fabrication. *Nano Lett.* (2020)

        doi:10.1021/acs.nanolett.0c03254.

60.   Cherian, C. T. *et al.* 'Bubble-Free' Electrochemical Delamination of CVD

        Graphene Films. *Small* **11**, 189–194 (2015).

61.   Hsieh, Y.-P., Kuo, C.-L. & Hofmann, M. Ultrahigh mobility in

        polyolefin-supported graphene. *Nanoscale* **8**, 1327–1331 (2016).

62.   Khabushev, E. M., Krasnikov, D. V., Kolodiazhnaia, J. V., Bubis, A. V. &

        Nasibulin, A. G. Structure-dependent performance of single-walled carbon nanotube

        films in transparent and conductive applications. *Carbon* **161**, 712–717 (2020).

63.   Derjaguin, B. V., Muller, V. M. & Toporov, Yu. P. Effect of contact deformations

        on the adhesion of particles. *J. Colloid Interface Sci.* **53**, 314–326 (1975).

64.   Melitz, W., Shen, J., Kummel, A. C. & Lee, S. Kelvin probe force microscopy and

        its application. *Surf. Sci. Rep.* **66**, 1–27 (2011).

65.   Piminov, P. A. *et al.* Synchrotron Radiation Research and Application at VEPP-4.

        Phys. Procedia **84**, 19–26 (2016).

66.   Krasnikov, D. V. *et al.* A spark discharge generator for scalable aerosol CVD

        synthesis of single-walled carbon nanotubes with tailored characteristics. *Chem. Eng.

        J.* **372**, 462–470 (2019).

67.   Strudwick, A. J. *et al.* Chemical Vapor Deposition of High Quality Graphene

Films from Carbon Dioxide Atmospheres. *ACS Nano* **9**, 31–42 (2015).

68.   Kim, C.-D., Min, B.-K. & Jung, W.-S. Preparation of graphene sheets by the reduction of carbon monoxide. *Carbon* **47**, 1610–1612 (2009).

69.   Chou, C. C. & Lin, C. I. Reaction between titanium dioxide and carbon in flowing helium stream. *Br. Ceram. Trans.* **100**, 197–202 (2001).

70.   Wu, Y. A. *et al.* Large Single Crystals of Graphene on Melted Copper Using Chemical Vapor Deposition. *ACS Nano* **6**, 5010–5017 (2012).

71.   Fan, Y., He, K., Tan, H., Speller, S. & Warner, J. H. Crack-Free Growth and Transfer of Continuous Monolayer Graphene Grown on Melted Copper. *Chem. Mater.* **26**, 4984–4991 (2014).

72.   Eren, B. *et al.* Activation of Cu(111) surface by decomposition into nanoclusters driven by CO adsorption. *Science* **351**, 475–478 (2016).

73.   Preobrajenski, A. B., Ng, M. L., Vinogradov, A. S. & Mårtensson, N. Controlling graphene corrugation on lattice-mismatched substrates. *Phys. Rev. B* **78**, 073401 (2008).

74.   Wilson, N. R. *et al.* Weak mismatch epitaxy and structural Feedback in graphene growth on copper foil. *Nano Res.* **6**, 99–112 (2013).

75.   Skoblin, G., Sun, J. & Yurgens, A. Encapsulation of graphene in Parylene. *Appl. Phys. Lett.* **110**, 053504 (2017).

76.   Zhukova, E. S. *et al.* Charge transport mechanisms in macro-scale CNT films. *J. Phys. Conf. Ser.* **1092**, 012178 (2018).

77.   Zhukova, E. S. *et al.* Terahertz-infrared electrodynamics of single-wall carbon nanotube films. *Nanotechnology* **28**, 445204 (2017).

78.   Gorshunov, B. P. *et al.* Terahertz spectroscopy of charge transport in films of pristine and doped single-wall carbon nanotubes. *Carbon* **126**, 544–551 (2018).

79.   Blanter, Ya. M. & Büttiker, M. Shot noise in mesoscopic conductors. *Phys. Rep.* **336**, 1–166 (2000).

80.   Piatrusha, S. U. *et al.* Noise Insights into Electronic Transport. *JETP Lett.* **108**, 71–83 (2018).

81.   Larionova, T. *et al.* Complex XPS and Raman Study of Graphene on Copper and Si/SiO2 Subjected to Ar Ion Treatment. *Key Engineering Materials* vol. 721 258–262 /KEM.721.258 (2017).

82.   Biesinger, M. C. Advanced analysis of copper X-ray photoelectron spectra. *Surf. Interface Anal.* **49**, 1325–1334 (2017).

83.   Henzler, K. *et al.* Investigation of reactions between trace gases and functional CuO nanospheres and octahedrons using NEXAFS-TXM imaging. *Sci. Rep.* **5**, 17729 (2015).

84.   Wahab, H. *et al.* The structural response of graphene on copper to surface- and interfacial-oxygen. *Carbon* **110**, 414–425 (2016).

85.   Avila, J. *et al.* Exploring electronic structure of one-atom thick polycrystalline graphene films: A nano angle resolved photoemission study. *Sci. Rep.* **3**, 2439 (2013).

86.   Pagliara, S. *et al.* Nature of the surface states at the single-layer graphene/Cu(111)

and graphene/polycrystalline-Cu interfaces. *Phys. Rev. B* **91**, 195440 (2015).

87.   Zhigunov, D. M. *et al.* Single-walled carbon nanotube membranes as non-reflective substrates for nanophotonic applications. *Nanotechnology* **32**, 095206 (2020).

88.   Grebenko, A. K. *et al.* Local ultra-densification of single-walled carbon nanotube films: modeling and experiment. *ArXiv220306387 Cond-Mat Physicsphysics* (2022).

89.   Ostanin, I., Ballarini, R., Potyondy, D. & Dumitrică, T. A distinct element method for large scale simulations of carbon nanotube assemblies. *J. Mech. Phys. Solids* **61**, 762–782 (2013).

90.   Ostanin, I., Dumitrică, T., Eibl, S. & Rüde, U. Size-Independent Mechanical Response of Ultrathin Carbon Nanotube Films in Mesoscopic Distinct Element Method Simulations. *J. Appl. Mech.* **86**, (2019).

91.   Notargiacomo, A. *et al.* Atomic force microscopy lithography as a nanodevice development technique. *NANOTECHNOLOGY* **10**, 458–463 (1999).